Mechanisms of wake evolution and aerodynamic interaction in a propeller–airframe system under hover and forward flight conditions

Sang Min Son, Da-bin Jung, Chan-Ho Song, Rho Shin Myong, Hakjin Lee[a)]

School of Aerospace Engineering, Gyeongsang National University, Jinju, Gyeongnam 52828, South Korea

[a)]Author to whom correspondence should be addressed: hlee@gnu.ac.kr

Abstract

Propeller–airframe interaction is a key source of unsteady aerodynamic loading and noise in urban air mobility, yet the role of blade number in this interaction remains unclear. This study numerically examined propeller-blade-number effects on aerodynamic and aeroacoustic interference in a propeller–airframe system. To resolve the complex wake dynamics and the resulting surface pressure fluctuations, a source–doublet panel method with a time-accurate vortex particle method was employed. The aeroacoustic characteristics were evaluated using Farassat's Formulation 1A of the Ffowcs Williams–Hawkings equation. The analysis was performed for a Da Jiang Innovation (DJI) 9443 propeller–airframe configuration with two, three, four, and five blades, under hover and forward-flight conditions. The results showed that increasing the blade number from two to four generally weakened direct propeller–airframe interaction, reducing the peak-to-peak variation of propeller aerodynamic loads and the power density of airframe surface-pressure fluctuations. Specifically, the four-bladed configuration emerged as the optimal configuration, achieving substantial loading-noise reductions of 5.4 dB and 9.2 dB in hover and forward-flight relative to the two-bladed baseline. However, an excessive increase in blade number reduced wake pitch spacing, which promoted meandering and highly irregular wake structures and thereby induced additional unsteady aerodynamic loads on the airframe. Under forward-flight conditions, the aeroacoustic analysis also identified acoustic cancellation in the even-bladed configurations with two and four blades. This phenomenon was driven by destructive interference between the out-of-phase acoustic pressure signals radiated from the propeller and airframe.

1. Introduction

Recently, urban air mobility (UAM), or advanced air mobility, has garnered considerable attention as a potential solution for alleviating urban transportation challenges, particularly traffic congestion and increasing mobility demand in densely populated areas. UAM vehicles are generally regarded as electric vertical takeoff and landing (eVTOL) aircraft equipped with distributed electric propulsion (DEP) systems and designed for hover, vertical takeoff and landing, and low-altitude passenger or cargo transport missions [1]. Because these vehicles are expected to operate repeatedly in noise-sensitive urban and suburban environments, their aerodynamic and aeroacoustic characteristics must be understood in relation to vehicle performance, public acceptance, and certification requirements. A comprehensive survey by the European Union Aviation Safety Agency identified safety and noise as major public-acceptance concerns for UAM operations [2]. For DEP-based UAM vehicles, aerodynamic and aeroacoustic behavior depends not only on the isolated characteristics of individual propulsors but also on the interactions induced by compact installation. Moreover, because UAM noise is radiated near communities and often contains pronounced tonal components, the physical mechanisms underlying unsteady loading and noise generation must be clarified before low-noise vehicle configurations can be developed rationally [3–6].

On many UAM platforms with DEP systems, multiple propulsors are installed within a compact footprint near wings, booms, fuselage components, or supporting arms. Consequently, the installed aerodynamic environment differs fundamentally from that of an isolated propeller. Compared with typical full-scale helicopter rotors, small-scale UAM propulsors generally operate at relatively low Reynolds numbers and may require high disk loading to generate the required thrust within a limited rotor diameter [7,8]. Under these conditions, the propeller wake can exhibit strong contraction, coherent helical tip-vortex trajectories, and highly concentrated vortical structures in the near wake. When the airframe lies within or near this wake region, the propeller wake can interact directly with adjacent structural components, generating azimuthally nonuniform induced-velocity fields, wake distortion, and periodic pressure fluctuations on nearby surfaces. These effects can modify the aerodynamic characteristics of both the propeller and airframe and can introduce additional tonal noise components associated with the blade passing frequency (BPF) [9,10]. Despite this importance, the aerodynamics of propeller–airframe interactions remain unclear, particularly with respect to wake evolution, wake impingement on the airframe, and the resulting unsteady aerodynamic behavior and noise performance. In particular, blade number directly affects the arrangement of the helical tip-vortex system, including the spacing between adjacent vortical structures. A detailed

analysis of propeller–airframe interaction as a function of blade number is therefore essential to clarify how wake development and airframe interference influence unsteady aerodynamic loading and noise generation.

In isolated-propeller configurations, propeller wake evolution and blade-number effects have been extensively studied. Beyond its geometric role, blade number modifies the spacing between helical tip vortices, interactions among adjacent vortex spirals, and development of wake instability. Felli et al. [11] experimentally investigated wake transition and far-wake evolution in propellers with different blade counts using time-resolved visualization and velocimetry measurements. Their results indicated that reduced inter-spiral spacing promotes mutual interaction, vortex grouping, and wake distortion during downstream wake development, inducing a transition from an initially coherent helical wake to a more irregular vortical structure. The effects of blade number on acoustic radiation in isolated rotors and propellers have also been examined. For instance, Jo et al. [12] numerically predicted tonal noise in low-Reynolds-number rotors and reported that blade-number variation modifies aerodynamic loading, thereby changing tonal-noise amplitude and harmonic content. Akiwate et al. [13] further examined the balance between tonal and broadband noise across blade numbers and tip Mach numbers, indicating that blade number can alter the dominant acoustic component. Li et al. [14] used Reynolds-averaged Navier–Stokes (RANS) simulations to investigate how blade number affects rotor aerodynamics and noise emission under hover conditions. They found that increasing the number of blades reduces the loading on each blade and weakens tip-vortex intensity, thereby reducing the loading-noise contribution. Baskaran et al. [15] measured noise levels from isolated propellers with two, three, and five blades under static-thrust and incoming-flow conditions. They reported that a larger number of blades can increase broadband noise at the same tip speed, whereas tonal noise decreases as the aerodynamic load is distributed over more blades. Collectively, these studies clarify how blade number affects isolated-propeller wake dynamics and noise radiation. However, this understanding remains largely confined to isolated configurations, wherein the propeller wake evolves without direct interference from nearby airframe components. In installed propeller–airframe designs, the helical wake system can impinge on the airframe, induce unsteady surface loading, and create additional noise sources. Consequently, blade-number effects cannot be interpreted solely from the wake evolution and acoustic characteristics of isolated propellers. Instead, a detailed analysis of propeller–airframe interaction as a function of blade number is required to clarify how blade-number-dependent wake development and airframe interference influence unsteady aerodynamic loading and noise generation.

In compact DEP installations, nearby airframe components are directly exposed to the unsteady rotor wake. Such installation effects can produce surface pressure fluctuations, tonal noise associated with BPF and its

harmonics, and unsteady loading on nearby structures. Accordingly, the design and analysis of UAM and multirotor configurations should account for airframe installation effects. Several researchers have clarified the acoustic importance of installation effects. For instance, Zawodny et al. [16] predicted rotor–airframe interaction noise in hover using RANS simulation [17] and the Ffowcs Williams–Hawkings (FW–H) acoustic analogy. They found that rotor–airframe spacing amplifies BPF harmonic noise and can make the airframe an acoustic contributor comparable to the rotor. Wu et al. [18] found that, under propeller–strut interaction, strong impulsive acoustic pressure signals originate from periodic unsteady loading created by the downstream strut disturbance and propeller wake. More recently, Boyang et al. [19] experimentally investigated rotor–arm interaction noise in single and contra-rotating eVTOL rotor configurations using anechoic microphone array measurements. They found that close arm placement amplifies tonal noise and higher-BPF harmonic levels through interaction-induced loading fluctuations, whereas arm length and placement can alter noise directivity through phase-cancellation effects. Collectively, these acoustic studies indicate that nearby structural components can contribute substantially to interactional noise. However, they primarily focused on radiated-noise variation caused by installation effects, while the interaction mechanisms associated with wake deformation and airframe surface loading remain partially unresolved. Further, Jiao et al. [20] and Kim et al. [21] investigated wake interaction phenomena around propeller–airframe configurations and found that blade passage and wake impingement can generate unsteady surface pressure fluctuations and strongly affect aerodynamic and acoustic characteristics. Their results indicated that the airframe can alter wake evolution, promote tip-vortex deformation and wake diffusion, and generate unsteady airframe loading; at small spacing, these effects can make airframe noise comparable to or stronger than rotor noise. Although these studies offered a more direct, wake-resolved interpretation of rotor–airframe or propeller–airframe interaction, they were largely limited to hover conditions, under which the wake develops primarily in the axial direction. Under forward-flight conditions, freestream velocity causes the wake to evolve into a skewed structure, thereby exposing the airframe to a different pattern of wake impingement and surface pressure fluctuations. However, blade-number effects on skewed propeller-wake evolution, the resulting unsteady pressure loading on the airframe, and loading-noise radiation in installed propeller–airframe configurations remain largely unexplored.

Table I summarizes representative studies on propeller wake dynamics and propeller–airframe interaction. The literature review identifies two major gaps. First, although blade number effects on wake stability, aerodynamic loading, and noise radiation have been studied in isolated propellers, these findings cannot be directly extended to installed propeller–airframe configurations. This is because the presence of the airframe

substantially alters wake development, vortex trajectories, and unsteady loading, thereby altering the underlying wake dynamics and noise-generation mechanisms. Second, previous rotor–airframe or propeller–airframe interaction studies have been conducted mainly under hover conditions and have focused primarily on rotor performance or overall noise levels. Consequently, the effects of wake evolution and wake impingement on airframe pressure loading and loading-noise radiation remain insufficiently resolved, particularly when the wake is deformed by the nearby airframe and evolves under forward-flight conditions. In particular, the present study reveals that an increased blade number promotes the onset of wake meandering, which induces pronounced low-frequency aerodynamic fluctuations. This complex wake dynamics fundamentally alters the acoustic contribution of the airframe, establishing it as a primary source of unsteady loading and interactional noise.

Table I. Representative aerodynamic and aeroacoustic studies of propeller–airframe interaction

Study	Model	Condition	Research focus
Felli et al. [11] (2011)	Isolated propeller	Hover	Wake physics with varying blade numbers
Baskaran et al. [15] (2023)	Isolated propeller	Hover	Acoustic characteristics with varying blade numbers
Zawodny et al. [16] (2020)	Propeller–airframe configuration	Hover	Prediction of the propeller and airframe noise
Kim et al. [21] (2024)	Propeller–airframe configuration	Hover	Interactional aerodynamics and acoustics of a propeller–airframe configuration
Present study	Propeller–airframe configuration	Hover and forward-flight	Wake-resolved analysis of the mechanisms associated with airframe loading and acoustic characteristics in propeller–airframe interaction

To address these gaps, this study investigates propeller–airframe interaction for two-, three-, four-, and five-bladed fixed-pitch propellers under hover and forward-flight conditions. For each blade-number configuration, the rotational speed is adjusted to maintain constant total thrust, allowing the aerodynamic and acoustic effects of blade number to be compared under a consistent thrust condition. A coupled framework based on a source–doublet panel method and the vortex particle method (VPM) are used to resolve unsteady wake development and propeller–airframe aerodynamic interaction, while Formulation 1A of Farassat based on the FW–H equation is employed to evaluate the loading-noise contributions from the propeller blades and airframe surface. The main objective of the present study is to elucidate the physical mechanism of blade number variation in modifying the

spacing and mutual interaction of helical tip vortices, as well as the subsequent impact of this wake reorganization on wake–airframe impingement, unsteady airframe loading, and loading-noise generation. Under forward-flight conditions, the analysis further examines the effects of a skewed wake, azimuthally asymmetric blade loading, and the phase interference between propeller and airframe acoustic pressure signals on the total interactional noise. Overall, the present results clarify the flow physics governing wake evolution and interactional aerodynamics in propeller–airframe systems for UAM applications, thereby providing practical guidance for future low-noise aircraft.

2. Numerical Methods

An in-house mid-fidelity solver coupling the source–doublet panel method, Lagrangian VPM, and Farassat's Formulation 1A of the FW–H equation was employed herein. Specifically, the source–doublet panel method was used to evaluate inviscid flow, surface pressure, and aerodynamic loads on the propeller blades and cylindrical airframe, whereas the VPM was used to model the wake as Lagrangian vortex particles. Notably, this framework enables analyses of tip-vortex trajectories, wake contraction, wake impingement, and the resulting unsteady aerodynamic interaction in compact propeller–airframe arrangements. Farassat's Formulation 1A was coupled with the aerodynamic solver to predict loading-noise components associated with unsteady aerodynamic forces obtained from the panel–vortex simulation. Previous studies have assessed the coupled aerodynamic–aeroacoustic framework for various rotor and propeller configurations. These validations have demonstrated that the solver can predict rotor aerodynamic loads, wake trajectories [22–26], and tonal-noise directivity [27,28] with reasonable accuracy across various rotor models and operating conditions. In particular, a previous study [28] using the same numerical framework included validation of rotor–fuselage interaction for the ROBIN configuration. The predicted unsteady fuselage surface pressure variations captured the characteristic 4/rev fluctuations induced by the four-bladed rotor, with phase and amplitude trends consistent with experimental measurements and reference computational results. Although the geometry differs from the present propeller–airframe configuration, this comparison provides supporting validation of the framework for wake-induced unsteady pressure loading on a nearby airframe surface. Additionally, the framework has been applied to multirotor [29–31] and full-configuration helicopter problems [32,33] involving strong wake interference, where it captured the relationship between unsteady aerodynamic loading and the resulting loading-noise characteristics. These prior validations and applications validate the use of this framework for the present canonical propeller–airframe problem,

particularly for propeller wake development, wake–airframe interaction, and the associated unsteady aerodynamic and aeroacoustic behavior.

2.1 Source-doublet panel method

The source–doublet panel method was used to evaluate aerodynamic loads on the propeller blades and cylindrical airframe. The corresponding formulation assumed inviscid, incompressible, and irrotational flow outside the solid boundaries; under this assumption, the perturbation velocity potential satisfied the Laplace equation. The propeller-blade and airframe surfaces were discretized into panel elements, and the velocity potential was represented by source, σ, and doublet, μ, singularity distributions on the body and wake surfaces. Using Green's second identity and assuming a constant potential inside the solid body, the boundary integral equation for the velocity potential was expressed as in Eq. (1).

$$-\frac{1}{4\pi}\iint_{S_B}\left[\sigma\left(\frac{1}{r}\right)-\mu\nabla\left(\frac{1}{r}\right)\boldsymbol{n}\right]dS+\frac{1}{4\pi}\mu\nabla\left(\frac{1}{r}\right)ndS=0\cdot \tag{1}$$

For numerical implementation, the source and doublet strengths were assumed constant over each panel. The integral equation was then discretized by introducing the geometric influence coefficients C_k and C_j for N body panels and N_w wake panels, yielding the algebraic form in Eq. (2). The source strength was determined from the Neumann boundary condition, which enforced the no-penetration condition on the body surface. In the time-marching simulation, this condition accounted for the relative velocity between the surface and surrounding flow, including the freestream velocity, translational motion, and blade rotation. The wake doublet strength, μ_w, was obtained from the Kutta condition at the blade trailing edge, where the jump in surface doublet strength defines the circulation shed into the wake. This shed circulation provided the initial vorticity information for the subsequent Lagrangian vortex-particle wake representation.

$$\sum_{k=1}^{N}C_k\mu_k+\sum_{j=1}^{N_W}C_j\mu_{W,j}-\sum_{k=1}^{N}C_k\mu_k=0\,, \tag{2}$$

The local velocity components at each collocation point on the blade and airframe surfaces were evaluated from the spatial derivatives of the velocity potential, including contributions from the body panels, wake panels, and vortex particles. The blade-surface pressure coefficient was then evaluated using the unsteady Bernoulli equation in Eq. (3). In this formulation, the blade-surface pressure coefficient, $C_{p,blade}$, was determined from the temporal variation of the velocity potential, ϕ, and the local velocity, $\boldsymbol{V}_{total}$, computed from the source and doublet singularities. To account for the unsteady flow induced by blade rotation, a time-dependent boundary condition

based on the kinematic velocity, $\boldsymbol{V}_{kinematic}$, was imposed on the blade surface. Notably, the kinematic velocity is defined as the sum of the freestream velocity, rotor rotational velocity, and relative blade-motion velocity, including the contribution from feathering.

$$C_{p,blade} = \frac{P_{blade} - P_\infty}{\frac{1}{2}\rho\left|\boldsymbol{V}_{kinematic}\right|^2} = 1 - \frac{\left|\boldsymbol{V}_{total}\right|^2}{\left|\boldsymbol{V}_{kinematic}\right|^2} - \frac{2}{\left|\boldsymbol{V}_{kinematic}\right|^2}\frac{\partial\phi}{\partial t}. \tag{3}$$

For the airframe surface, pressure variation induced by the propeller wake was evaluated using a pressure reconstruction procedure based on the Poisson equation for the specific stagnation enthalpy, B, as expressed in Eq. (4). In this formulation, the bound-circulation contribution from the blade and the wake vorticity were incorporated into the surface pressure reconstruction.

$$4\pi B + \iint_S B\frac{\partial}{\partial n}\left(\frac{1}{r}\right)dS = \int_{blade}\frac{\boldsymbol{r}\cdot(\boldsymbol{V}_B\times\Gamma dl)}{r^3} + \iiint_{wake}\frac{\boldsymbol{r}\cdot((\boldsymbol{V}_\infty+\boldsymbol{v})\times\boldsymbol{\omega})}{r^3}, \tag{4}$$

where S denotes the airframe surface, B denotes the specific stagnation enthalpy on the airframe surface, $\boldsymbol{r}$ is the position vector from the source point to the airframe collocation point; $\boldsymbol{r} = |r|$ is its magnitude; and n is the outward normal to the surface. The first term on the right-hand side represents the pressure contribution from the bound circulation on the propeller blade, where Γ is the bound circulation vector and $\boldsymbol{V}_\mathrm{B}$ is the local velocity associated with the blade-bound vortex system. The second term represents the wake-vorticity contribution, where $\boldsymbol{\omega}$ is the vorticity carried by the vortex particles and $\boldsymbol{V}_\omega$ is the corresponding local convection velocity. Thus, Eq. (4) reconstructs the specific stagnation enthalpy on the airframe surface by incorporating both the propeller-blade bound circulation and the vorticity field of the convecting wake. The reconstructed specific stagnation enthalpy, B, was then converted into the airframe surface pressure coefficient, $C_{p,airframe}$, using Eq. (5).

$$C_{p,airframe} = \frac{P_{airframe} - P_\infty}{\frac{1}{2}\rho\left|\boldsymbol{V}_{kinematic}\right|^2} = 1 - \frac{\left|\boldsymbol{V}_{total}\right|^2}{\left|\boldsymbol{V}_{kinematic}\right|^2} - \frac{2B}{\left|\boldsymbol{V}_{kinematic}\right|^2}, \tag{5}$$

where $P_{airframe}$ and P_∞ denote the local static pressure on the airframe and the reference pressure, respectively, and ρ is the air density. Thus, Eq. (5) relates the pressure distribution on the cylindrical airframe to the propeller-induced velocity field and the wake-induced enthalpy variation reconstructed from Eq. (4).

2.2 Vortex particle method

Complex propeller wakes and their interactions with nearby airframe components are important sources of unsteady aerodynamic loading and tonal noise in compact rotorcraft and UAM configurations. Herein, the VPM

was used to model the propeller wake as a set of discrete Lagrangian vortex particles [34]. By enabling individual vortex particles to convect independently with the local velocity field, the VPM can retain coherent vortical structures with relatively low numerical dissipation and describe the temporal evolution of the propeller wake without a background volume grid. Unlike free-wake methods based on vortex filaments, the VPM does not require prescribed connectivity between adjacent wake elements. This feature is particularly valuable for the present propeller–airframe problem because the propeller wake can deform substantially and impinge on the airframe surface. Accordingly, the VPM was coupled with the source–doublet panel method, ensuring that propeller-blade bound circulation, airframe aerodynamic influence, and free-wake evolution were treated within the same time-marching framework. In the present analysis, the VPM represented the propeller wake, whereas the wake generated by viscous separation from the cylindrical airframe was not modeled as vortex particles. Consequently, the analysis focused on the interaction between the propeller wake and the airframe, rather than on bluff-body wake shedding from the airframe itself.

The convection velocity of each vortex particle was evaluated as the linear superposition of the freestream velocity, $\boldsymbol{V}_{\infty}$, and the induced-velocity contributions from the propeller blades, $\boldsymbol{V}_{ind,blade}$; shed wake elements, $\boldsymbol{V}_{ind,filament}$; and previously released vortex particles, $\boldsymbol{V}_{ind,particle}$, as expressed in Eq. (6).

$$\boldsymbol{V}_{convect}(s_m,t)=\boldsymbol{V}_{\infty}+\boldsymbol{V}_{induced,blade}+\boldsymbol{V}_{induced,filament}+\boldsymbol{V}_{induced,particle}. \tag{6}$$

The particle positions were then advanced in time using a second-order Runge–Kutta scheme, allowing the wake geometry to evolve in response to the instantaneous induced-velocity field. The wake flow field was discretized into a collection of Lagrangian vortex particles, p, each carrying vector-valued vorticity, α_n. The velocity induced at the location of the mth particle by all other particles, $n = 1, 2, \ldots, p$ and $n \neq m$, was evaluated using the regularized Biot–Savart law in Eq. (7), where x_m denotes the position of the mth particle.

$$\boldsymbol{V}_{induced,particle}(\boldsymbol{x}_m,t)=-\sum_{n=1}^{p}\frac{1}{\sigma_{mn}^{3}}K(\rho)(\boldsymbol{x}_m-\boldsymbol{x}_n)\times\alpha_n \tag{7}$$

A regularized kernel formulation, K, was used to prevent singular behavior in the induced-velocity field at short interparticle distances. Here, ρ is the interparticle distance normalized by the symmetric core parameter σ_{mn}. The function $G(\rho)$ denotes the regularized Green function associated with the vector stream function, and $\xi(\rho)$ represents the radially symmetric smoothing function used to distribute vorticity over a finite vortex core. The vortex core was modeled using the three-dimensional high-order algebraic smoothing function proposed by Winckelmans and Leonard [34] which yields a smooth vorticity distribution while retaining the induced-velocity

behavior required for wake convection. This regularization is essential for maintaining numerical stability when particles approach one another during wake contraction, distortion, or airframe-induced wake deformation.

$$K(\rho) = \frac{G(\rho) - \xi(\rho)}{\rho}. \tag{8}$$

Because direct evaluation of particle–particle interactions scales as $O(N^2)$, Message-Passing-Interface-based parallel computation was used to reduce computational cost while retaining full pairwise interactions among vortex particles.

2.3 FW–H acoustic analogy

The aeroacoustic analysis was performed using the FW–H acoustic analogy, which has been widely used for rotor and propeller noise prediction. Here, Farassat's Formulation 1A was adopted with the impermeable-surface formulation. Because the considered panel–vortex aerodynamic solver yielded the motion of solid surfaces and unsteady surface loading, the impermeable FW–H formulation allowed acoustic pressure to be decomposed into thickness and loading-noise components, corresponding to the monopole contribution associated with surface displacement and the dipole contribution associated with unsteady aerodynamic loading. With the impermeable surface defined on the solid boundaries, the acoustic integration included both the propeller blade surfaces and cylindrical airframe surface. Including both surfaces allowed the acoustic contribution of the airframe to be evaluated together with that of the rotating propeller blades, which is important for the present propeller–airframe configuration.

In propeller–airframe arrangements, the propeller wake periodically impinges on nearby airframe components and generates unsteady surface pressure fluctuations. These fluctuations introduce additional loading-noise components associated with the airframe surface and can modify the tonal components associated with the BPF and its harmonics. Accordingly, the formulation was used to predict noise radiated from the propeller blades and to examine the relative contribution of the airframe surface to the interactional noise field. In the present study, only the loading-noise component is considered because the main focus is the unsteady aerodynamic loading induced by propeller–airframe interaction. The loading-noise pressure, P'_L, at an observer location is evaluated from the surface integral of the unsteady aerodynamic loading, as expressed in Eq. (9). In this equation, ρ_0 denotes the ambient density, a_0 denotes the speed of sound, and r denotes the distance between the acoustic source and the observer. The variable l_r denotes the radiation-direction component of the aerodynamic loading. All source quantities are evaluated at the retarded time to account for the finite propagation speed of sound from the moving

source surface to the observer. However, the present framework does not directly resolve viscous boundary-layer development, flow separation, or turbulence-related acoustic sources. Consequently, boundary-layer noise, separation-induced broadband noise, and quadrupole noise are not included in the present acoustic predictions.

$$p'_L(\boldsymbol{x},t) = \frac{1}{4\pi a_0}\int_{f=0}\left[\frac{\dot{l}_r}{r\left|1-M_r\right|^2}\right]_{ret} dS + \frac{1}{4\pi}\int_{f=0}\left[\frac{l_r - l_M}{r^2\left|1-M_r\right|^2}\right]_{ret} dS + \frac{1}{4\pi a_0}\int_{f=0}\left[\frac{l_r(r\dot{M}_r + a_0 M_r - a_0 M^2)}{r^2\left|1-M_r\right|^3}\right]_{ret} dS \tag{9}$$

Notably, the present impermeable FW–H formulation predicts deterministic thickness and loading noise associated with prescribed surface motion and unsteady aerodynamic loading. Although thickness noise is included as an inherent component of the acoustic signature, the present analysis emphasizes loading-noise characteristics because mutual propeller–airframe interaction produces unsteady aerodynamic loading on both the blade and airframe surfaces, which acts as a primary noise source in propeller–airframe configurations. Consequently, quadrupole noise components and other stochastic broadband components are not directly modeled in the present framework. This exclusion represents a limitation of the present acoustic analysis because the intensified flow field generated by propeller–airframe interaction may also contribute to broadband noise radiation through turbulence, surface boundary-layer fluctuations, and separated flow structures. A more comprehensive assessment of these broadband noise mechanisms requires high-fidelity resolution of the surrounding flow field and a permeable FW–H formulation, both of which lie beyond the scope of this study.

3. Numerical Setup

3.1 Propeller–airframe configuration

The Da Jiang Innovation (DJI) 9443 propeller [35,36] was selected as the baseline model for investigating propeller–airframe interaction in a compact rotorcraft configuration. Because this propeller has been widely used in small-scale unmanned aerial vehicle (UAV) studies, it provides a suitable reference geometry for analyzing propeller aerodynamics and wake evolution. The DJI 9443 propeller was also selected because its aerodynamic and aeroacoustic characteristics have been validated using numerical frameworks related to those used in the present study. For instance, Lee and Lee [29] predicted the acoustics of an isolated DJI 9443 propeller using the FW–H-based noise solver employed here. The predicted directivity patterns of the first and second BPF components agreed well with experimental measurements, and this agreement across different rotational speeds

demonstrated the capability of the numerical framework to predict DJI 9443 propeller noise. Additionally, Kim et al. [21] investigated the interaction between the DJI 9443 propeller and simplified cylindrical and conical airframes using high-fidelity lattice Boltzmann method (LBM) simulations under hovering conditions. Their results indicated that a nearby airframe can substantially increase the radiated noise level and that the airframe surface can serve as an important acoustic contributor in propeller–airframe configurations. Building on these studies, the present study used the same DJI 9443 propeller and a cylindrical airframe as a canonical configuration to examine how blade-number variation influences wake evolution, wake impingement on the airframe, and interactional aerodynamics under hover and forward-flight conditions.

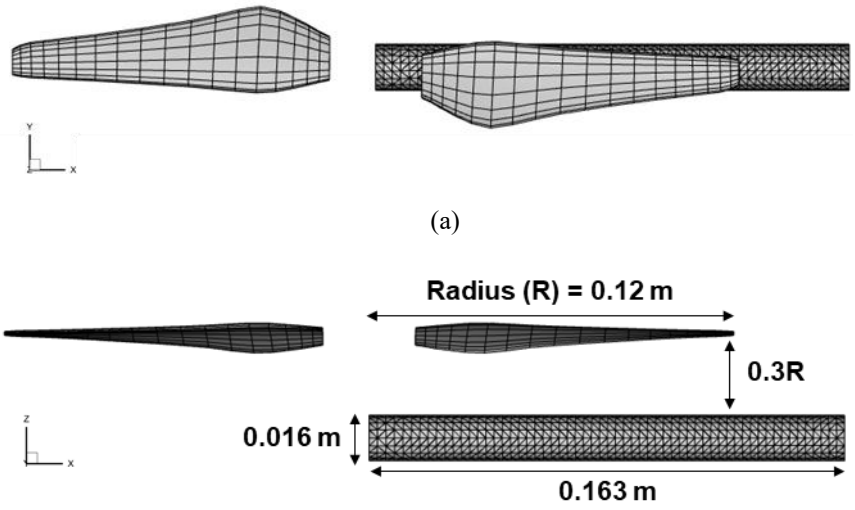

Fig. 1. Geometry and surface discretization of the DJI 9443 propeller and airframe for the source–doublet panel method: (a) surface-panel discretization and (b) side-view arrangement with key geometric dimensions.

Table II. Geometric specifications of the DJI 9443 propeller and airframe

Parameter	Value
Blade radius	0.12 m
Reference aspect ratio	4.26
Root cutoff	15%
Airframe length	0.163 m
Airframe radius	0.008 m
Propeller–airframe distance	0.036 m

Fig. 1 displays the geometric configuration used in the present study, and Table II summarizes the corresponding geometric specifications. The propeller radius was R = 0.12 m, and the reference aspect ratio was 4.26. Although the original DJI Phantom 2 propulsion system uses a two-bladed propeller, the present study considered blade-number variation to examine how wake structure affects propeller–airframe interaction. To create propeller models with different blade numbers while maintaining consistent blade-root treatment, the root cutoff was set to 15% of the propeller radius. The airframe was idealized as a cylindrical body with a length of 0.163 m, radius of 0.008 m, and diameter of 0.016 m. This simplified cylindrical geometry represents a canonical airframe or support-arm component placed near a propeller, allowing the wake–airframe interaction to be isolated from additional geometric complexity. The cylinder was positioned beneath the propeller disk with a vertical clearance of 0.3R, corresponding to 0.036 m, so that the propeller wake could interact directly with the airframe surface. Both the propeller blades and cylindrical airframe were discretized using surface panels for the source–doublet panel method, as illustrated in Fig. 1. This figure shows the surface mesh distribution on the blades and cylinder, together with the relative propeller–airframe spacing.

3.2 Simulation setup

Herein, blade number was the primary parametric variable and was varied from two to five to examine its effects on wake evolution, wake–airframe interaction, and the resulting aerodynamic and aeroacoustic characteristics under hover and forward-flight conditions. To enable a consistent comparison among blade-number configurations, the total thrust of the propeller–airframe system was fixed at 3 N for all cases. Because the DJI 9443 propeller has fixed-pitch blade geometry, rotational speed was used as the trim variable to satisfy the target thrust rather than applying collective or cyclic pitch inputs. Because the blade radius was identical for all configurations, this thrust-trim procedure produced different rotational speeds and tip Mach numbers across blade numbers. Consequently, the present results should be interpreted as a constant-thrust comparison of fixed-pitch propeller–airframe configurations, not as a comparison at the same rotational speed or tip Mach number. Table III summarizes the rotational speeds obtained from the thrust-trim procedure under hover and forward-flight conditions at V_∞ = 10 m/s. The propeller rotated counterclockwise when viewed from above. The azimuth angle was defined such that ψ = 0° corresponds to the blade position directly above the cylinder centerline. Forward-flight was prescribed along the negative x-axis, parallel to the cylinder axis, as presented in Fig. 1.

Table III. Rotational speeds obtained from the thrust-trim procedure for the propeller–airframe configuration

Condition	Two blades	Three blades	Four blades	Five blades
Hover	6,080 rpm	5,800 rpm	4,850 rpm	4,650 rpm
Forward-flight	5,010 rpm	4,110 rpm	3,730 rpm	3,050 rpm

In the coupled source–doublet panel/VPM framework, temporal resolution and surface-panel discretization directly affect the blade-bound circulation distribution and the vorticity shed into the particle wake. Accordingly, these numerical parameters were defined before the wake–airframe interaction analysis because the phase, strength, and trajectory of the propeller wake strongly influence the unsteady loading on the airframe. To assess both aerodynamic and aeroacoustic sensitivity, the resolution study was conducted using an isolated two-bladed DJI 9443 propeller in hover at 5,400 rpm, for which experimental thrust and acoustic data were available from Zawodny et al. [35]. In addition to thrust, the 1st BPF SPL was evaluated at five microphone locations distributed from $\theta = -45°$ to 45° at 22.5° intervals. The acoustic sensitivity was quantified using the mean absolute error of the predicted 1st BPF SPL relative to the experimental measurements over these five microphone locations. Time-step and surface-panel resolutions were examined sequentially, as summarized in Tables IV and V.

Table IV. Results of the time-step resolution study of the isolated two-bladed DJI 9443 propeller

Case	Azimuthal step size ($\Delta\psi$)	Thrust	Thrust error relative to experimental measurements	1st BPF SPL error relative to experimental measurements	Computational time
1	5°	2.62 N	11.3 %	3.27 dB	0.5 h
2	2°	2.45 N	4.0 %	2.95 dB	7.2 h
3	1°	2.50 N	6.2 %	2.74 dB	55.0 h

Table V. Results of the surface-panel resolution study of the isolated two-bladed DJI 9443 propeller

Case	Blade surface grid (Chordwise/Spanwise)	Thrust	Thrust error relative to experimental measurements	1st BPF SPL error relative to experimental measurements	Computational time
1	9/11	2.45 N	4.0 %	2.95 dB	7.2 h
2	18/21	2.32 N	1.4 %	2.08 dB	13.1 h
3	27/31	2.36 N	0.4 %	1.89 dB	23.3 h

The results of the time-step resolution study are summarized in Table IV. Each blade was discretized using a 9 × 11 panel grid in the chordwise and spanwise directions. Under this condition, three azimuthal step sizes, $\Delta\psi$ = 5°, 2°, and 1°, were examined; these corresponded to 72, 180, and 360 time steps per revolution, respectively. Case 1, with $\Delta\psi$ = 5°, required only 0.5 h of computational time but overpredicted thrust at 2.62 N, producing an 11.3% error relative to the experimental measurement. The corresponding mean absolute error of the 1st BPF SPL was 3.27 dB. Refining the azimuthal step size to $\Delta\psi$ = 2° in Case 2 reduced the thrust error to 4.0% and the 1st BPF SPL error to 2.95 dB, although the computational time increased to 7.2 h. In Case 3, the temporal resolution was further refined to $\Delta\psi$ = 1°; the 1st BPF SPL error was slightly reduced to 2.74 dB, whereas the thrust error increased to 6.2% and the computational time rose sharply to 55 h. Thus, further refinement from $\Delta\psi$ = 2° to 1° provided only a small improvement in acoustic prediction while substantially increasing the computational cost and did not improve the thrust prediction. Consequently, Case 2 was selected because it offered the best compromise among aerodynamic and acoustic accuracy and computational efficiency. The azimuthal step size of $\Delta\psi$ = 2°, corresponding to 180 time steps per revolution, was therefore used for all subsequent simulations.

Using the selected temporal resolution of $\Delta\psi$ = 2°, a surface-panel resolution study was then conducted for the isolated propeller, and the results are summarized in Table V. Three blade-surface discretizations were examined: 9 × 11, 18 × 21, and 27 × 31 panels in the chordwise and spanwise directions, respectively. Case 1, which used the coarsest 9 × 11 panel grid, predicted a thrust of 2.45 N with an error of 4.0%, while the mean absolute error of the 1st BPF SPL was 2.95 dB; the computational time was 7.2 h. Increasing the blade-surface resolution to 18 × 21 panels in Case 2 improved the thrust prediction to 2.32 N and reduced the thrust error to 1.4%. The 1st BPF SPL error was also reduced to 2.08 dB, with a moderate increase in computational time to 13.1 h. Case 3, which used the finest 27 × 31 panel grid, produced the smallest thrust and acoustic errors of 0.4% and 1.89 dB, respectively, but increased the computational time to 23.3 h. Both the thrust and 1st BPF SPL results, therefore, showed improved agreement with the experimental measurements as the surface resolution was refined. However, the additional refinement from Case 2 to Case 3 yielded only a marginal improvement in both aerodynamic and acoustic predictions, despite the increase in computational time. Consequently, the 18 × 21 panel discretization of Case 2 was adopted for subsequent simulations as a balanced resolution for blade loading, wake generation, and acoustic prediction.

After the temporal and blade-surface resolutions were selected, the thrust of the isolated two-bladed DJI 9443 propeller in hover was predicted at rotational speeds of 4,800, 5,400, and 6,000 rpm. As shown in Fig. 2, the present panel-method predictions were compared with the experimental measurements and OVERFLOW2 CFD

results based on unsteady RANS simulations reported by Zawodny et al. [35] The predicted thrust agreed well with the experimental data across the tested rotational-speed range, with a maximum deviation of less than 3.3%. The comparison further revealed that the present panel-method results were comparable to the OVERFLOW2 computational fluid dynamics (CFD) predictions. Together, these results support the reliability of the numerical framework with the selected temporal and spatial resolutions for predicting DJI 9443 propeller thrust. In addition to the aerodynamic validation, Fig. 2(b) compares the predicted and measured 1st BPF SPLs at five observer locations from θ = -45° to 45°. The predicted SPL distributions follow the measured variation with elevation angle at 4,800, 5,400, and 6,000 rpm, including the change in acoustic level with rotational speed. These results provide complementary validation of the dominant tonal loading-noise prediction using the selected temporal and spatial resolutions.

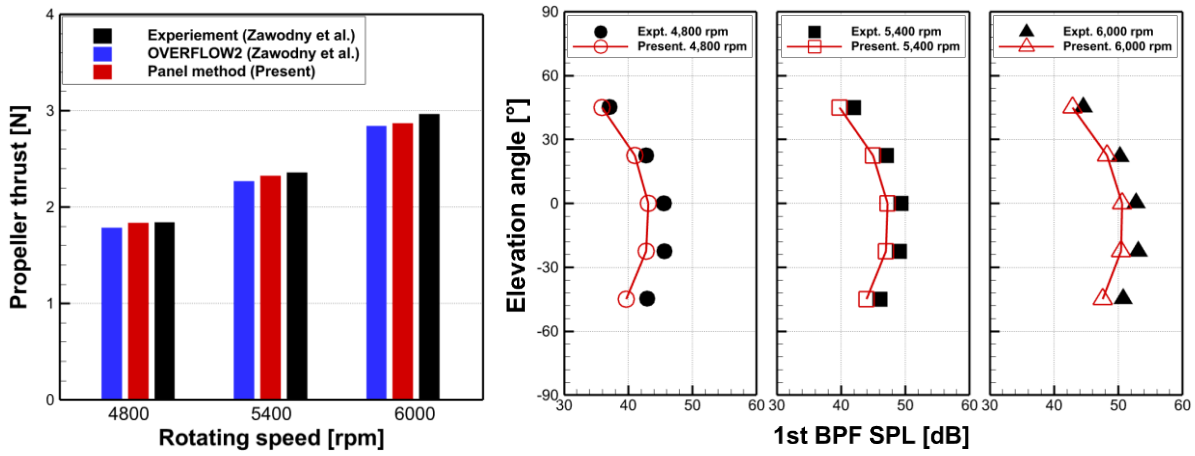

(a) (b)

Fig. 2. Validation of isolated two-bladed DJI 9443 propeller in hover at rotational speeds of 4,800, 5,400, and 6,000 rpm: (a) Propeller thrust, (b) 1st BPF SPL.

3.3 Acoustic setup

The time-resolved aerodynamic results derived from the coupled panel–vortex simulation were used as inputs for the FW–H acoustic analysis. The unsteady aerodynamic calculations were performed with an azimuthal step size of $\Delta\psi$ = 2°, and each simulation was conducted for 14 propeller revolutions. Once the wake and surface-loading characteristics reached a developed state, aerodynamic source data from the final five revolutions were used for the acoustic analysis. A source-duration sensitivity assessment using three to seven revolutions showed that the five-revolution history produced maximum differences of 0.005 dB and 0.419 dB at the first and second BPFs, respectively, relative to the seven-revolution result. These differences support the use of the five-revolution

source history for resolving the dominant BPF-related loading-noise components considered in the present study, consistent with the spectral resolutions adopted in previous small-rotor acoustic studies [37,38]. A source-time-dominant algorithm was used to relate the source emission time to the observer reception time, and the acoustic-pressure histories at the observer locations were reconstructed at uniform time intervals by linear interpolation before spectral analysis. Sound pressure level spectra were obtained by applying a fast Fourier transform to the acoustic-pressure histories recorded at the observer locations. To reduce spectral leakage, a Hann window was applied with 50% overlap during spectral averaging.

The microphones were placed on a circular arc in the x–z plane to evaluate the acoustic directivity of the propeller–airframe system. 24 observer locations were uniformly distributed at 15° intervals on a circle of radius $15R$, corresponding to 1.8 m, centered at the propeller hub. The elevation angle $\theta = 0°$ corresponds to the observer in the positive x-direction, whereas $\theta = 90°$ and $\theta = 270°$ correspond to the positive and negative z-directions, respectively. The observer at $\theta = 180°$ is located in the negative x-direction. The same observer arrangement was used for both hover and forward-flight conditions to allow a consistent comparison of noise directivity.

4. Results and Discussion

This section details how blade-number variation affects the interactional aerodynamics, wake evolution, and noise characteristics of the propeller–airframe system. Two-, three-, four-, and five-bladed configurations are compared under the constant-thrust condition defined in Sec. 3.2. Accordingly, the results should be interpreted as comparisons among constant-thrust, fixed-pitch propeller–airframe configurations rather than as blade-number comparisons at a fixed tip Mach number. The analysis first considers hover, under which the propeller wake impinges on the cylindrical airframe in a primarily periodic manner. It then considers forward-flight to clarify the additional effects of wake skewing, asymmetric wake convection, and modified wake–airframe impingement. Across both operating conditions, the analysis emphasizes the physical connection among wake development, surface-loading variation, and the resulting noise-generation characteristics.

4.1 Hover condition

The hover-condition analysis first considers the wake structure because the organization of the propeller wake near the cylindrical airframe governs the subsequent propeller loading, airframe loading, surface-pressure distribution, and aeroacoustic characteristics. Fig. 3 presents the instantaneous wake structures and vorticity-

magnitude contours for the two-, three-, four-, and five-bladed configurations at $\psi = 0°$, corresponding to the blade-passage phase at which one blade is closest to the airframe. The left panels present the Lagrangian vortex-particle wake structures, while the right panels present the vorticity-magnitude contours in the x–z plane through the airframe centerline. Together, these views characterize the three-dimensional helical wake organization and the near-airframe vortical field governing local interaction with the cylindrical body. In the left panels of Fig. 3, vortex-particle size is scaled according to the vorticity strength carried by each particle. Thus, concentrated tip vortices generated by strong vorticity near the blade tip are represented by relatively large particles, whereas the weaker trailing vortex sheet shed from the blade span is represented by smaller particles.

In the two-bladed configuration, only two blades produced the total thrust, so each blade carried higher aerodynamic loading. The corresponding increase in bound circulation generated stronger shed and trailing vorticity, forming pronounced helical tip-vortex structures in the near wake. Because only two blades released vortical structures during one revolution, the azimuthal separation between successive blade wakes was relatively large**.** This represents the initial stage of tip-vortex development, in which coherent helical vortices form downstream of the blade tips and convect toward the cylindrical airframe. As the blade number increased from two to four, the required loading per blade decreased, reducing the resulting tip-vortex strength and near-wake vorticity level. Concurrently, the spacing between consecutive blade wakes decreased because more blades shed vortical structures within one rotor revolution. Accordingly, blade-number variation produced two competing effects: reduced vortex strength associated with lower blade loading and reduced spiral-to-spiral distance associated with the increased number of helical wake traces. For the three- and four-bladed configurations, the reduced spacing between successive helical vortices increases their mutual interaction during downstream convection. However, the concurrent reduction in individual vortex strength allows the wake to remain comparatively organized as it approaches the airframe.

In the five-bladed configuration, the smaller spiral-to-spiral distance produces stronger interaction among adjacent vortical structures. As the wake approaches the airframe, neighboring vortex trajectories exhibit greater local convergence and deformation, followed by a pronounced loss of regular helical organization near and below the cylindrical body. This behavior aligned with the wake-instability mechanism discussed by Felli et al. [11]. The proximity of the cylindrical airframe further influenced the interaction because the descending helical wake encountered the airframe within the near field.

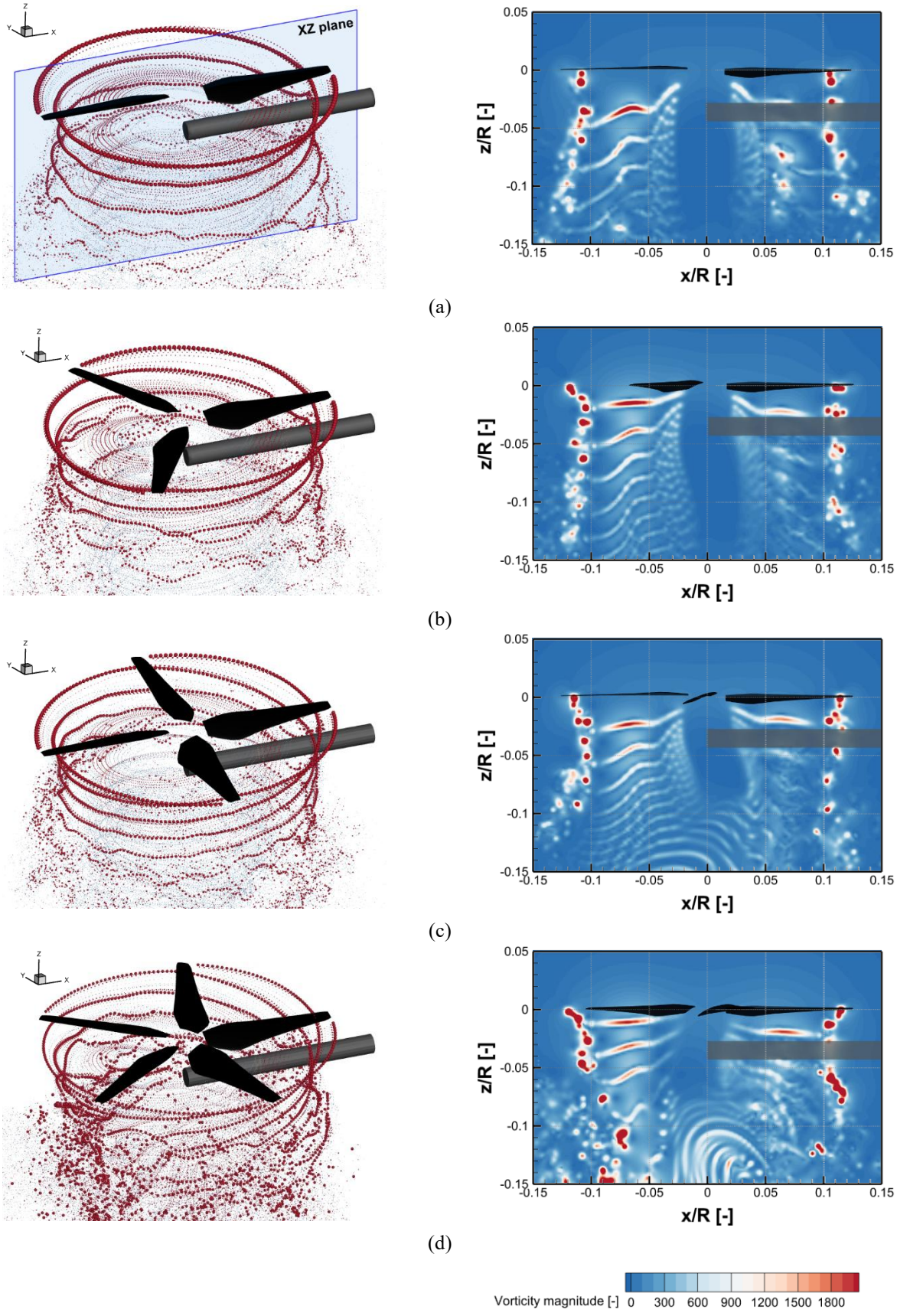

Fig. 3. Instantaneous Lagrangian vortex particle wake structures (left) and vorticity magnitude contours on the *x*–*z* plane passing through the airframe centerline (right) under hover conditions at $\psi = 0°$: (a) two-bladed, (b) three-bladed, (c) four-bladed, and (d) five-bladed configurations

In particular, a local loss in regular helical organization appeared in the positive x/R region adjacent to the airframe, indicating premature breakdown and distortion of the helical wake structure near the cylinder [39,40]. As the descending tip vortices impinged on the upper surface of the airframe, local shear and wake deformation promoted secondary-vorticity formation around the upper and lateral portions of the cylindrical surface. Consequently, the five-bladed wake no longer maintained a regular sequence of coherent tip-vortex traces near the cylinder; instead, adjacent vortical structures became locally distorted and spatially uneven. Further, the reduced pitch distance between consecutive tip vortices intensified their mutual interaction, and and local convergence near the airframe. This interaction was accompanied by lateral wake deflection in the lower region, which produced a highly irregular, skewed near-field flow structure [11]. The vorticity contours also indicated a nonuniform distribution of concentrated vortical regions around the lower and lateral portions of the airframe, suggesting that wake impingement was governed by the collective arrangement of adjacent helical vortices rather than by a single blade passage event. Together, the wake structures in Fig. 3 provide the physical basis for interpreting the loading characteristics discussed in the following sections. Increasing the blade number simultaneously reduces the strength of individual tip vortices and decreases the spacing between successive helical structures. The resulting balance between weaker individual vortices and stronger interaction among adjacent vortical structures determines the subsequent wake evolution. Therefore, the comparatively organized three- and four-bladed wakes are associated with weaker loading fluctuations, whereas the stronger mutual interaction and wake deformation observed in the five-bladed configuration introduce additional variations in wake impingement and airframe loading.

To complement the qualitative wake visualization in Fig. 3, the tip vortex trajectories were compared between the two- and five-bladed configurations, which exhibited the most distinct wake evolution features among the blade-number configurations. The trajectories were obtained by identifying Lagrangian vortex particles shed from the blade-tip region and tracking their positions as they convected through the wake. Two representative trajectories were selected based on the shedding azimuth, ψ_s=0° and 180°, corresponding to the airframe side and the opposite side of the rotor disk, respectively. The radial position was defined as $r/R=\sqrt{x^2+y^2}/R$, whereas the vertical position was defined as z/R. The wake age was defined as ψ_w, where t_s denotes the vortex shedding time. Fig. 4 presents the resulting radial and vertical tip-vortex trajectories as functions of wake age. Here, ψ = 0° corresponds to the azimuthal position on the airframe side, where the blade passes above the cylindrical body, whereas ψ = 180° corresponds to the opposite side of the rotor disk. Therefore, the difference between the ψ = 0°

and ψ = 180° trajectories provides a quantitative measure of asymmetric wake evolution caused by the airframe. Overall, the comparison demonstrated that the two- and five-bladed configurations exhibited fundamentally different wake trajectory characteristics rather than merely different fluctuation amplitudes.

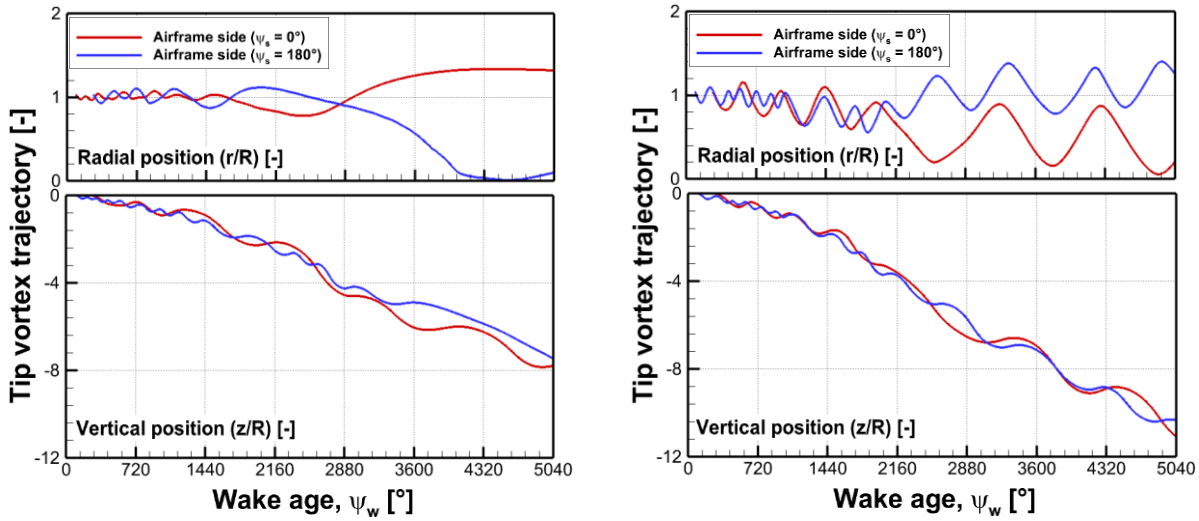

Fig. 4. Radial and vertical trajectories of tip vortices shed from the airframe-side (ψ_S=0°) and opposite-side (ψ_S =180°) blade positions under hover conditions: (a) two-bladed and (b) five-bladed configurations. The trajectory coordinates are normalized by the propeller radius and plotted as functions of wake age, ψ_W.

For the two-bladed configuration in Fig. 4(a), the radial trajectories at ψ = 0° and ψ = 180° displayed only limited lateral displacement across the analyzed wake region. The difference between the two azimuthal positions became more evident downstream, indicating that the cylindrical airframe introduced asymmetric distortion into the otherwise helical wake contraction as the tip vortices convected near the body. Nonetheless, compared with the five-bladed case in Fig. 4(b), the two-bladed wake had a relatively small radial displacement and maintained a coherent helical trajectory despite the asymmetric influence of the cylindrical body. In the vertical direction, both trajectories indicated similar downward convection of the tip vortices. Although small trajectory differences appeared between the airframe side and the opposite side, the overall vertical motion remained regular, indicating that the airframe distorted the two-bladed wake locally but did not substantially alter its helical trajectory.

Meanwhile, the five-bladed configuration in Fig. 4(b) exhibited markedly different behavior. In the radial direction, the trajectory displayed large-amplitude, nearly periodic lateral displacement, and the difference between ψ = 0° and ψ = 180° was much more pronounced than in the two-bladed case [41,42]. This behavior indicates that the five-bladed wake did not simply undergo regular helical contraction but instead displayed strong lateral wandering of the tip vortex trajectory. The vertical trajectory of the five-bladed configuration also differed from that of the two-bladed case. The larger vertical displacement of the tip vortex trajectory in the five-bladed

configuration was attributed primarily to evaluation at the same wake age in rotor revolutions rather than at the same physical time. Because the five-bladed configuration used a lower rotational speed to maintain the same propeller thrust condition, reaching the same number of revolutions required a longer physical time and consequently led to greater vertical wake convection. While mean downward convection of the tip vortices was still observed, the trajectory featured distinct oscillatory variations superimposed on the downward motion. These trajectory variations indicated that vertical wake development was affected not only by the propeller-induced slipstream but also by mutual interaction among closely spaced helical vortices and local disturbance introduced by the airframe. This wake behavior is consistent with the large-scale wake displacement reported in previous rotor and propeller wake studies [43,44]. The corresponding low-frequency variation of the tip-vortex trajectories is also consistent with the low-frequency fluctuations observed in the propeller thrust and airframe forces of the five-bladed configuration. Additional isolated-propeller simulations showed that the five-bladed wake develops a loss of regular helical organization even without the airframe, whereas the two-bladed wake remains comparatively coherent over the same near-wake region. The presence of the airframe further increases the deformation of the five-bladed wake, suggesting that the reduced spacing between adjacent vortical structures and the airframe disturbance both contribute to the observed wake evolution. However, the sensitivity of this behavior to vortex-particle regularization and numerical dissipation was not independently quantified; therefore, a numerical contribution to the downstream wake irregularity cannot be excluded. The low-frequency variation of the tip-vortex trajectories is consistent with the corresponding fluctuations observed in the propeller thrust and airframe forces, which are also reflected in the low-frequency surface-pressure component in Fig. 7.

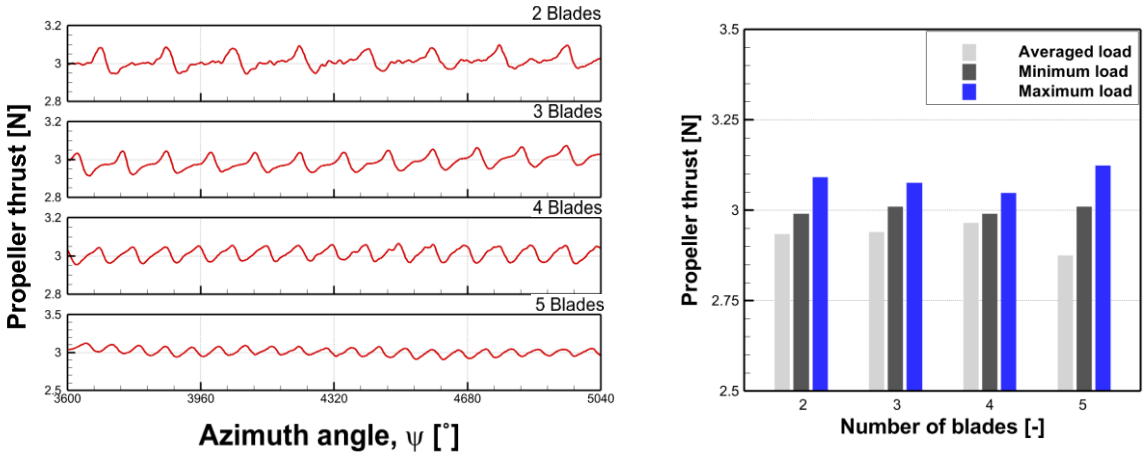

Fig. 5. Propeller thrust characteristics under hover for different blade-number configurations: (a) thrust time histories over the final four revolutions and (b) minimum, mean, and maximum thrust values.

Following the wake-structure analysis, unsteady propeller loading was examined to determine how wake interaction near the airframe influenced thrust fluctuations under hover conditions. Fig. 5 compares the thrust histories from the final four revolutions of the simulation with the corresponding minimum, mean, and maximum thrust values. As depicted in Fig. 5(a), the thrust trim procedure maintained the mean propeller thrust near the 3 N target for all blade-number configurations. Therefore, the differences in thrust history mainly reflected changes in unsteady loading associated with blade passage and wake–airframe interaction rather than differences in mean thrust. In the two-, three-, four-, and five-bladed configurations, periodic thrust fluctuations associated with blade-passing events were observed. The dominant fluctuation occurred at N_b/rev, where N_b is the number of blades, because each blade periodically passed over the cylindrical airframe and experienced a local blockage effect similar to the ground-effect mechanism. As the blade approached the airframe, the propeller-induced downward flow was partially obstructed by the cylindrical surface, producing a local upwash region between the blade and the airframe. This upwash increased the effective angle of attack for the blade section passing above the airframe and thereby produced a transient increase in blade loading. This periodic loading variation produced the blade-number-dependent thrust oscillations observed in Fig. 5(a). In the two- and three-bladed cases, additional small-amplitude fluctuations were superimposed on the dominant blade-passing component, suggesting that the interaction was governed not only by instantaneous blade–airframe proximity but also by the passage of previously shed vortical structures near the airframe. This interpretation is consistent with the wake structures shown in Fig. 3, where relatively coherent vortical structures remain near the airframe and can contribute to blade-passage-induced loading.

Fig. 5(b) further summarizes the thrust fluctuation amplitudes. Although the mean thrust remained nearly constant across the configurations, the minimum–maximum thrust range varied substantially with blade number. From the two- to four-bladed configurations, the peak-to-peak thrust variation decreased progressively. This reduction is consistent with the weakened tip vortex structures in Fig. 3, because lower loading per blade reduced the transient loading increase during blade passage over the airframe. In particular, the four-bladed configuration exhibited the smallest thrust variation, with a peak-to-peak amplitude ~47.5% lower than that of the two-bladed case. However, the five-bladed configuration exhibited an interaction feature distinct from those observed in the two- to four-bladed cases. In the five-bladed configuration, stronger mutual interaction among the neighboring vortical structures shown in Fig. 3 modified the phase and intensity of wake impingement on the cylindrical airframe over successive revolutions, thereby producing low-frequency blade-loading variation. This behavior was reflected in the low-frequency thrust variation and increased peak-to-peak thrust fluctuation shown in Fig.

5(b). Thus, increasing blade number reduced blade-passing-related loading fluctuations up to the four-bladed case, while the five-bladed case introduced additional unsteadiness associated with the collective organization of closely spaced helical tip vortices.

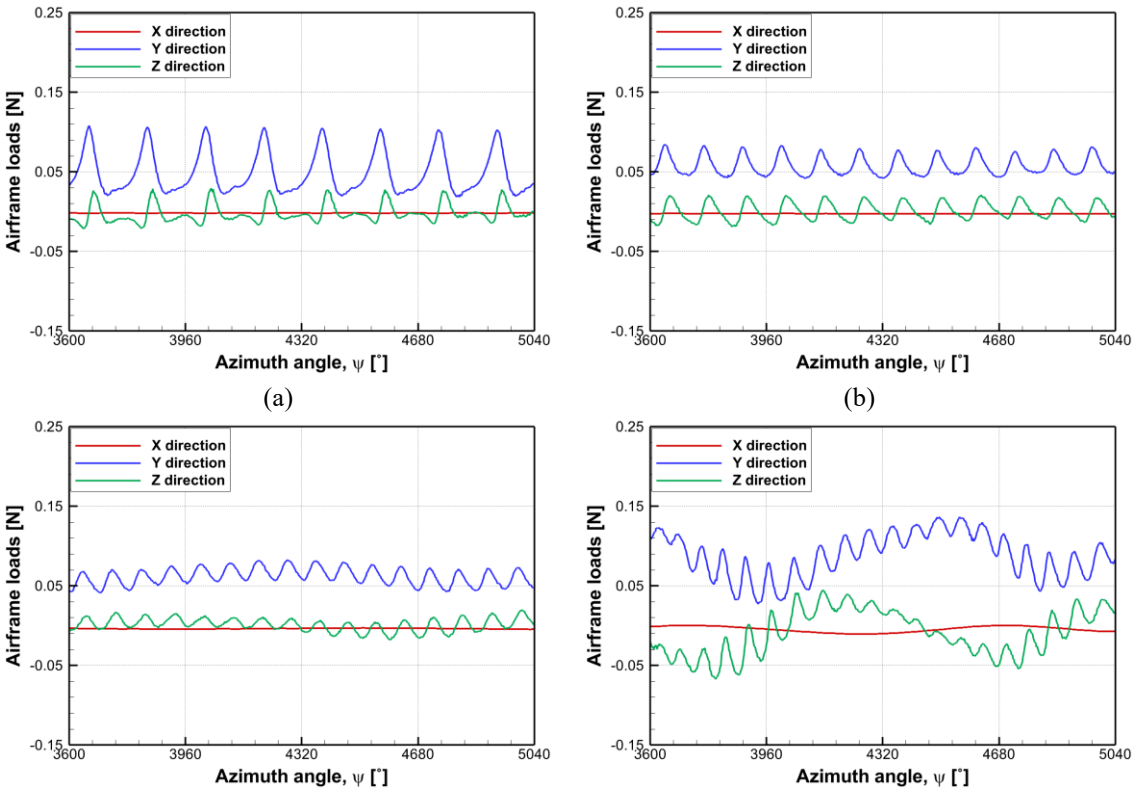

Fig. 6. Temporal histories of aerodynamic force components acting on the cylindrical airframe under hover conditions for different blade-number configurations: (a) two-bladed, (b) three-bladed, (c) four-bladed, and (d) five-bladed configurations.

Airframe loading was then examined to clarify how propeller wake impingement and blade-passing motion influenced unsteady aerodynamic forcing on the stationary cylindrical body. Fig. 6 presents the time histories of the aerodynamic force components acting on the airframe in the global coordinate system over the final four revolutions. The *x*- and *y*-directions correspond to the longitudinal and lateral airframe directions, respectively, whereas the *z*-direction is normal to the propeller disk plane, as defined in Fig. 1. Unlike propeller thrust, which was constrained by the thrust trim procedure, the airframe force components directly reflected the unsteady pressure field generated by blade passage and wake impingement on the cylindrical surface [20]. For the two-, three-, and four-bladed configurations, the airframe force histories displayed highly repeatable periodic fluctuations synchronized with blade-passing events. The dominant fluctuation frequency increased with blade number, consistent with the corresponding BPF. Meanwhile, the fluctuation amplitudes generally decreased from

the two- to four-bladed cases. This reduction is consistent with the wake structures identified in Fig. 3, where the tip vortex strength and near-wake vorticity level decreased from the two- to four-bladed configurations. It is also consistent with the propeller thrust variation in Fig. 5, where the blade-passage-related loading fluctuation became less pronounced as blade number increased from two to four. These trends indicate that the localized pressure imbalance on the cylindrical airframe weakened as the per-blade loading decreased. By contrast, the five-bladed configuration exhibited distinct airframe loading behavior. Additionally, a pronounced low-frequency variation appeared in both the *y*- and *z*-force components alongside the expected 5/rev fluctuation. This low-frequency force variation is consistent with the low-frequency thrust variation observed in Fig. 5, indicating that the unsteady interaction responsible for the propeller-side loading variation was also reflected in the airframe surface loading. As illustrated in Fig. 3, the five-bladed wake displayed a reduced spiral-to-spiral distance, local distortion of adjacent helical tip vortices, and a spatially uneven vortical field near the airframe. These wake features produced a time-varying impingement pattern on the cylindrical surface, causing a spatially uneven pressure response that appeared as low-frequency variations in the airframe force components. Among the three force components, the lateral *y*-force was dominant for all blade-number configurations. This dominance was attributed to the asymmetric pressure distribution generated as the rotating blades and their shed wakes passed over the laterally offset cylindrical airframe. As a blade moved into and out of the vicinity of the cylinder, local blockage and wake impingement produced an alternating pressure gradient along the lateral direction. Consequently, the *y*-force contained a stronger blade-passing-related fluctuation than the *x*- and *z*-force components.

Fig. 7 presents power spectral density (PSD) contours of the surface pressure fluctuations along the upper centerline of the cylindrical airframe. Surface pressure histories were extracted from $x/L = 0$ to 1 with a uniform spacing of $0.1L$. For the airframe length of $L = 0.163$ m, this corresponds to a spatial sampling interval of 0.0163 m. The frequency was normalized by the per-revolution order, such that 1/rev corresponds to the rotational frequency and the BPF occurs at N_b/rev, where N_b is the number of blades. The sectional spectra contained distinct energy concentrations at the BPF and its harmonics, although the harmonic intensity generally decreased at higher frequencies. For all blade-number configurations, the strongest pressure fluctuations were concentrated near ($x/L \approx 0.6$–0.8), corresponding to the primary wake-impingement footprint where blade passage and descending tip-vortex structures most strongly affected the local surface pressure. At higher harmonics, the high-energy region became increasingly localized toward $x/L \approx 0.8$, indicating that high-frequency pressure fluctuations were generated primarily by localized blade-passage and wake-impingement events.

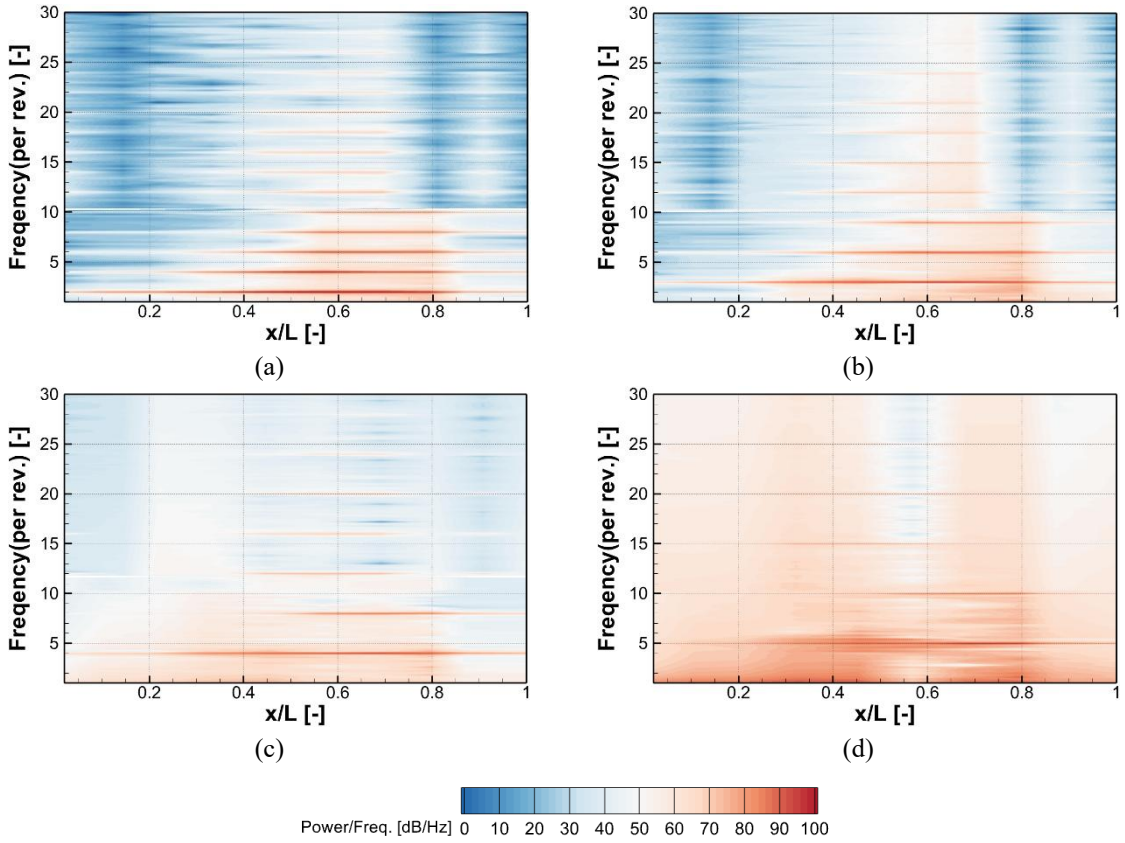

Fig. 7. Power spectral density (PSD) contours of surface pressure fluctuations along the upper centerline of the cylindrical airframe under hover conditions for different blade-number configurations: (a) two-bladed, (b) three-bladed, (c) four-bladed, and (d) five-bladed configurations. Frequency is normalized by the shaft frequency, with the BPF corresponding to N_b/rev.

For a quantitative comparison, the PSD levels were extracted at x/L = 0.7, within the primary wake-impingement region. In the per-revolution representation, 1/rev corresponds to the shaft frequency and the BPF occurs at N_b/rev. The BPF PSD levels decrease from 103.70 dB/Hz for the two-bladed configuration to 97.40, 96.25, and 95.38 dB/Hz for the three-, four-, and five-bladed configurations, respectively. The reduction becomes more pronounced at higher harmonics: the 2BPF level decreases from 94.28 to 81.58 dB/Hz between the two- and five-bladed configurations, while the corresponding 3BPF level decreases from 91.44 to 59.96 dB/Hz. These results quantitatively show the progressive weakening of the blade-passing-related pressure fluctuations, particularly at higher harmonics.

However, the five-bladed configuration exhibited a different spectral distribution. Although the discrete high-frequency harmonic content was less pronounced, the low-frequency energy became stronger and was distributed over a broader portion of the airframe. In contrast, the 1/rev component reaches 84.84 dB/Hz in the five-bladed configuration, compared with 66.11 dB/Hz in the four-bladed configuration. The enhanced spectral level therefore occurs primarily at low frequency rather than at the BPF harmonics, consistent with the resolved low-frequency

wake motion and the corresponding aerodynamic-load variations identified in Figs. 4–6. The increased low-frequency PSD in the five-bladed configuration is associated with the low-frequency wake motion observed in Figs. 3 and 4. The reduced spacing between adjacent tip vortices enhances their mutual interaction, resulting in radial and vertical variations of the wake trajectory. These variations alter the wake impingement on the airframe over successive revolutions and produce low-frequency surface-pressure fluctuations in addition to the nominal 5/rev loading. Thus, unlike the two- to four-bladed configurations, the five-bladed case contains an additional low-frequency component associated with the resolved wake motion. This low-frequency component represents resolved wake-induced variations in aerodynamic loading and should not be interpreted as turbulence-induced broadband noise, which is not directly modeled in the present framework. Therefore, the present discussion is limited to loading-noise characteristics associated with the resolved propeller–airframe interaction.

The influence of blade-number variation on the loading-noise directivity of the propeller–airframe system was examined under hover conditions. Specifically, the acoustic contributions of each component were compared. Because the present study focuses on the influence of blade-number variation on unsteady aerodynamic loading and wake-induced surface-pressure fluctuations, only the loading-noise component was considered in the acoustic analysis. For small drone propellers with thin blades and moderate tip Mach numbers, previous studies have shown that the thickness-noise contribution can be neglected or excluded when the primary interest is the loading-noise mechanism [35,45]. Therefore, the present analysis examined the loading noise radiated from both the rotating propeller blades and the stationary cylindrical airframe.

Fig. 8 presents the predicted loading-noise directivity evaluated at observer locations spaced every 15° in elevation angle around the propeller–airframe system for each blade-number configuration. From the two- to four-bladed configurations, the propeller loading-noise level decreased, consistent with the reduced thrust fluctuation observed in Fig. 5. However, in the five-bladed configuration, the propeller loading-noise level increased again in the out-of-plane directions, particularly near $\theta = 90°$ and 270°. The tip vortex trajectory in Fig. 4 indicated stronger radial wandering and vertical trajectory oscillation, and the low-frequency thrust variation in Fig. 5 indicated that blade loading contained a component beyond the nominal 5/rev blade-passing fluctuation. Together, these wake-trajectory variations modified wake impingement and intensified unsteady loading on the propeller blades, thereby enhancing dipole radiation in the out-of-plane directions. Thus, the reduction in propeller loading-noise level observed from the two- to four-bladed configurations was not sustained in the five-bladed case.

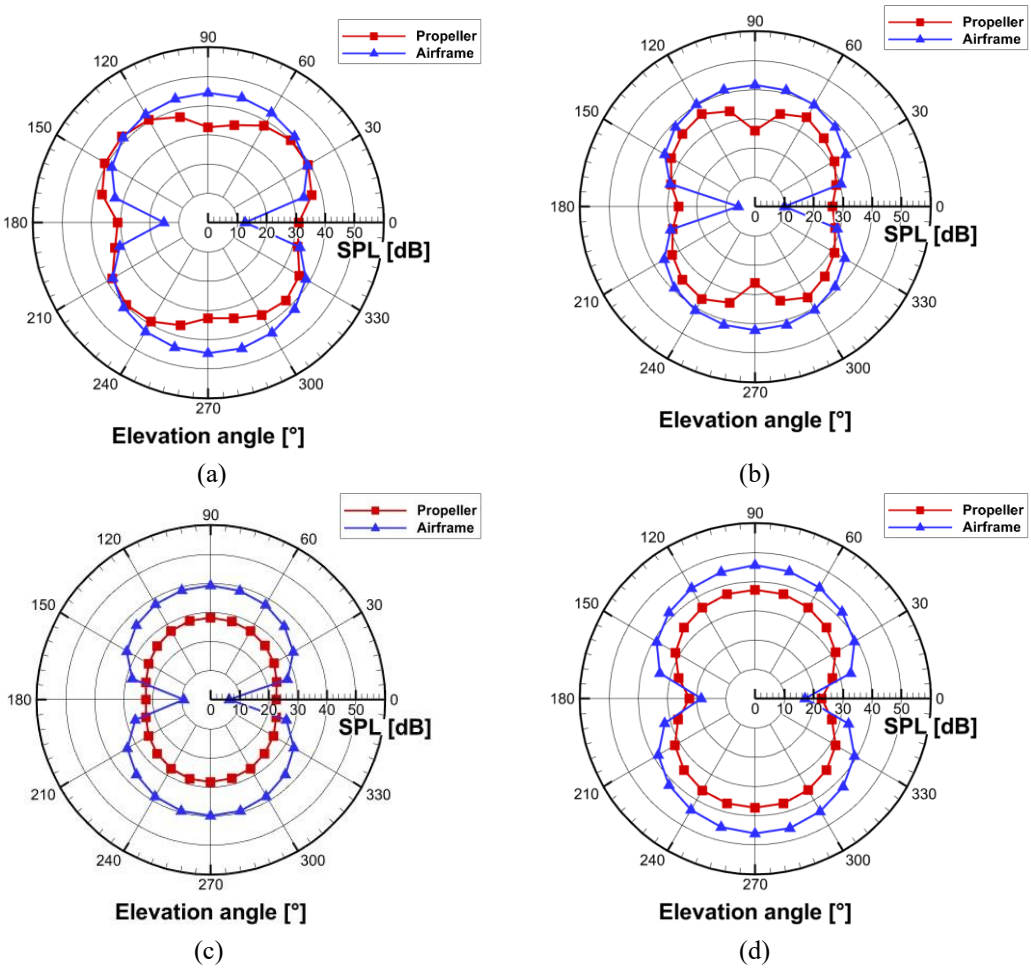

Fig. 8. Directivity of loading noise radiated from the propeller and cylindrical airframe under hover conditions for different blade-number configurations: (a) two-bladed, (b) three-bladed, (c) four-bladed, and (d) five-bladed configurations.

The directivity patterns in Fig. 8 indicated that the airframe contribution exhibited more pronounced dipole directivity than the propeller contribution, with stronger radiation toward the upper and lower observer regions near θ = 90° and 270°. This airframe directivity behavior reflected the unsteady surface loading generated by blade passage and wake impingement on the stationary cylindrical body, consistent with the out-of-plane radiation characteristics of dipole loading noise [19]. Consequently, the airframe made a comparable or larger contribution to the loading noise than the propeller over a wide range of elevation angles, except near the propeller in-plane region. The relative directivities of the propeller and airframe reveal a distinct feature of the two-bladed configuration. Near θ = 15°, 165°, and 195°, the propeller contribution locally exceeds that of the airframe. Because the prescribed total thrust is supported by only two blades, the larger loading carried by each blade produces stronger blade-passing-related loading fluctuations, consistent with the thrust history in Fig. 5. As the

blade number increases, these fluctuations decrease and the local dominance of the propeller is no longer evident. In contrast, the airframe contribution remains strongest near θ = 90° and 270°, reflecting the unsteady surface loading generated by blade passage and wake impingement on the stationary cylindrical body, as also indicated by the airframe force and surface pressure results in Figs. 6 and 7.

This contribution was attributed to the strong unsteady aerodynamic forcing imposed on the stationary airframe by the nearby propeller wake. As indicated in Fig. 6, this wake–airframe interaction produced pronounced unsteady aerodynamic forces on the airframe in all three directions, indicating that the airframe surface contributed to the unsteady loading associated with loading-noise generation. Using high-fidelity LBM simulations, Kim et al. [21] similarly reported that airframe noise can exceed propeller noise when the propeller and airframe are placed close together. As their separation increases, the interaction weakens, wake-induced aerodynamic forces on the airframe decrease, and the airframe noise level is consequently reduced. Therefore, the present results indicate that the airframe becomes an important loading noise source when strong wake–airframe interaction occurs in the propeller–airframe arrangement [16].

Table VI. Comparison of predicted loading-noise levels under hover conditions at θ = 270° for different blade-number configurations

	Two blades	Three blades	Four blades	Five blades
Propeller OASPL	33.33 dB	26.06 dB	28.22 dB	37.27 dB
Airframe OASPL	45.29 dB	42.18 dB	39.84 dB	46.10 dB
Total OASPL	45.37 dB	41.28 dB	40.20 dB	45.84 dB

Table VI presents the quantitative comparison of overall sound pressure level (OASPL) at θ = 270°, where unsteady loading-noise radiation was pronounced. For all blade-number configurations, the airframe contribution was greater than the propeller contribution, confirming that the stationary cylindrical airframe was the dominant loading-noise source under the present close propeller–airframe arrangement. The airframe OASPL decreased from 45.29 dB in the two-bladed configuration to 42.18 dB and 39.84 dB in the three- and four-bladed configurations, respectively. The propeller OASPL also decreased substantially from 33.33 dB in the two-bladed case to 26.06 dB in the three-bladed case, although it increased slightly to 28.22 dB in the four-bladed case. Consequently, the total OASPL decreased from 45.37 dB to 41.28 dB and 40.20 dB as blade number increased from two to four, with the four-bladed configuration yielding the lowest total OASPL and a 5.17 dB reduction

relative to the two-bladed case. However, the five-bladed configuration exhibited a clear increase in both propeller and airframe contributions. The propeller and airframe OASPLs increased to 37.27 dB and 46.10 dB, respectively, resulting in the highest total OASPL among the tested cases, at 45.84 dB. This total OASPL corresponded to a 5.64 dB increase relative to the four-bladed configuration. Therefore, the comparison confirmed that increasing blade number reduced the overall loading-noise level only up to the four-bladed configuration, whereas the five-bladed configuration produced additional unsteady loading associated with the distinct propeller–airframe interaction.

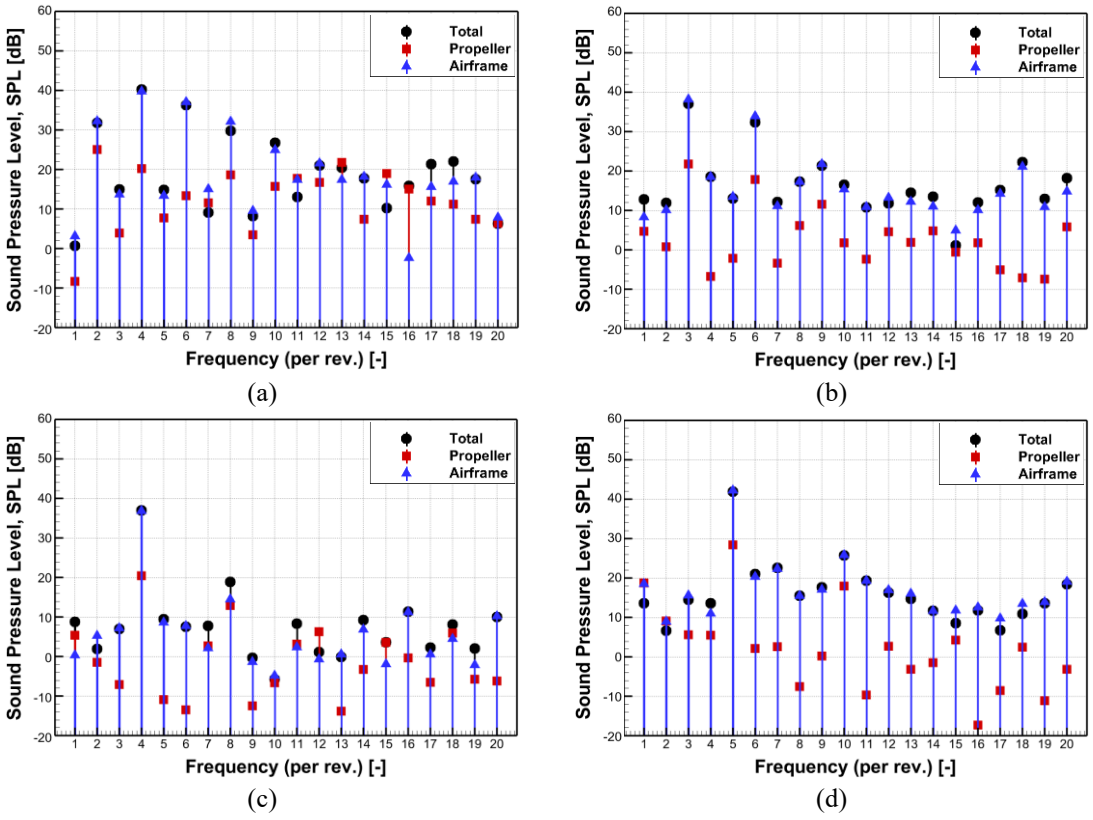

Fig. 9. Far-field loading-noise spectra of the propeller and cylindrical airframe at $\theta = 270°$ under hover conditions: (a) two-bladed, (b) three-bladed, (c) four-bladed, and (d) five-bladed configurations. Frequency is expressed in per-revolution order, where 1/rev represents one cycle per propeller revolution.

Fig. 9 presents the far-field loading-noise spectra of the propeller and cylindrical airframe at θ=270° under hover conditions for the different blade-number configurations. The frequency is expressed in per-revolution order, with the corresponding BPFs located at 2/rev, 3/rev, 4/rev, and 5/rev for the two-, three-, four-, and five-bladed configurations, respectively. Distinct tonal components were observed at the BPFs and their harmonics for both the propeller and airframe contributions.

From the two- to four-bladed configurations, the BPF-related spectral components generally decreased as the per-blade aerodynamic loading and the associated periodic loading fluctuations were reduced. This tendency is consistent with the reductions in propeller thrust and airframe surface pressure fluctuations identified in Figs. 5–7. In contrast, the five-bladed configuration exhibited enhanced spectral content below its nominal BPF of 5/rev. In particular, the propeller contribution showed an increased 1/rev component, while the airframe contribution exhibited elevated spectral levels over the range of approximately 1–4/rev. These sub-BPF components are consistent with the resolved low-frequency wake motion identified in Figs. 3 and 4, which introduced low-frequency variations in both propeller thrust and airframe loading. Consequently, the five-bladed configuration exhibited increased low-frequency loading-noise radiation from both the propeller and airframe, despite the reduction in per-blade loading. This result indicates that the high-blade-number acoustic response cannot be explained by RPM reduction alone, but is also influenced by blade-number-dependent wake dynamics and the resulting unsteady loading.

4.2 Forward-flight

The forward-flight condition was analyzed to clarify how blade-number variation influenced wake evolution and aerodynamic interactions in the propeller–airframe system. The freestream velocity was set to 10 m/s in the negative x-direction, with the freestream aligned with the longitudinal axis of the cylindrical airframe. Because the propeller had fixed-pitch blade geometry, no collective or cyclic pitch input was used for trim, even under forward-flight conditions. Instead, the prescribed total thrust was maintained by adjusting the rotational speed for the two-, three-, four-, and five-bladed configurations, as summarized in Table III. Figs. 10 and 11 present the phase-averaged vorticity-magnitude contours on the x–z and y–z planes, respectively, at $\psi = 0°$. The phase-averaged fields were obtained by averaging the flow fields at the same blade azimuth over the final three propeller revolutions. This treatment reduces cycle-to-cycle variation while preserving the blade-phase-dependent wake features relevant to the present analysis. Unlike under the hover condition, the freestream convected the propeller wake downstream along the airframe axis, producing a skewed wake structure that strongly interacted with the cylindrical airframe. Therefore, under forward-flight conditions, the wake–airframe interaction was governed by the combined effects of periodic blade passage, wake impingement on the airframe, streamwise wake distortion, and azimuthally nonuniform wake convection.

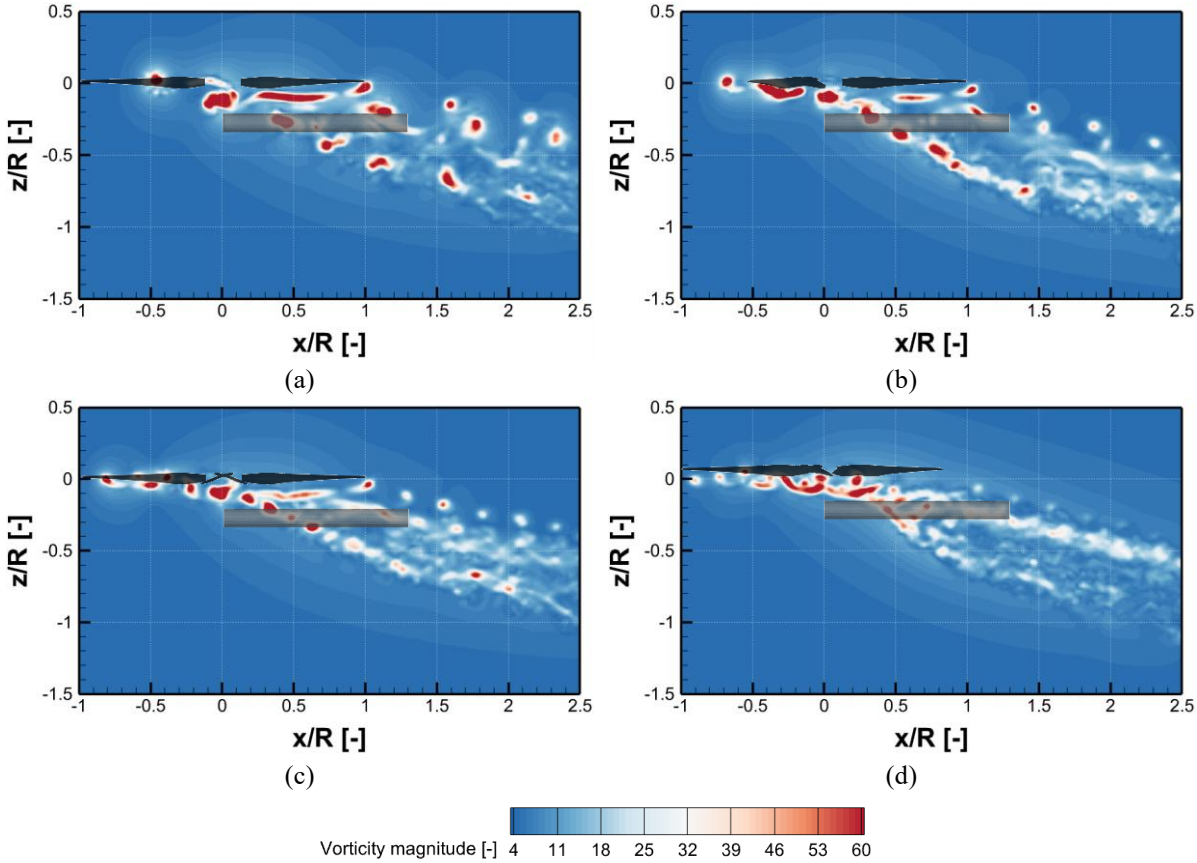

Fig. 10. Phase-averaged vorticity magnitude contours on the *x*–*z* plane under forward-flight conditions at ψ = 0°: (a) two-bladed, (b) three-bladed, (c) four-bladed, and (d) five-bladed configurations.

Specifically, as depicted in Fig. 10, the vorticity field was examined on the *x*–*z* plane at *y*/*R* = 0.5, corresponding to the advancing-side region where propeller tip vortex structures were clearly represented under forward-flight. In Fig. 10, the phase-averaged vorticity field is shown on the *x*–*z* plane at *y*/*R* = 0.5, corresponding to the advancing-side region where the propeller tip-vortex structures are clearly represented under forward-flight conditions. Evaluating the field at ψ = 0° allows the persistent blade-phase-dependent wake characteristics to be compared among the different blade-number configurations. The vorticity contours indicated that the skewed wake was convected downstream toward the aft and lower regions of the airframe. Unlike under the hover condition, where wake impingement was concentrated near the blade-passage region of the airframe at *x*/*L* ≈ 0.5–0.8, the propeller wake interacted with a much broader portion of the cylindrical body. Among the blade-number configurations, the two-bladed configuration produced the most distinct and concentrated vortical structures, consistent with higher per-blade loading under the constant-thrust condition. In the two-bladed case, a relatively coherent skewed helical wake was maintained over the near-field region up to approximately *x*/*R* = 2.5. However, as blade number increased, both per-blade loading and the vorticity magnitude decreased. Concurrently, the

reduced spiral-to-spiral distance enhanced wake-to-wake interaction in the four- and five-bladed configurations, leading to less distinct helical tip-vortex structures and a more fragmented near-wake organization. Thus, the blade-number effect should be interpreted as a combined change in vortex strength and wake interaction, rather than as a simple reduction in vortex strength. The vertical position of the wake also varied with blade number. In the higher blade-number configurations, the dominant vortical structures were displaced farther toward the lower side of the airframe, and the concentrated tip vortex structures became less distinct below the cylinder. This increased downward wake displacement was associated with enhanced mutual interaction among adjacent helical vortices, which altered the convection path of the forward-flight skewed wake near the airframe. In the five-bladed configuration, the reduced spiral-to-spiral distance further promoted mutual interaction among adjacent helical tip vortices before they convected around the airframe, making the downward-displacement effect more pronounced. Consequently, the wake reached the airframe with a spatially nonuniform organization, modifying the location and phase of wake impingement and generating a more complex vortical structure near the cylindrical body.

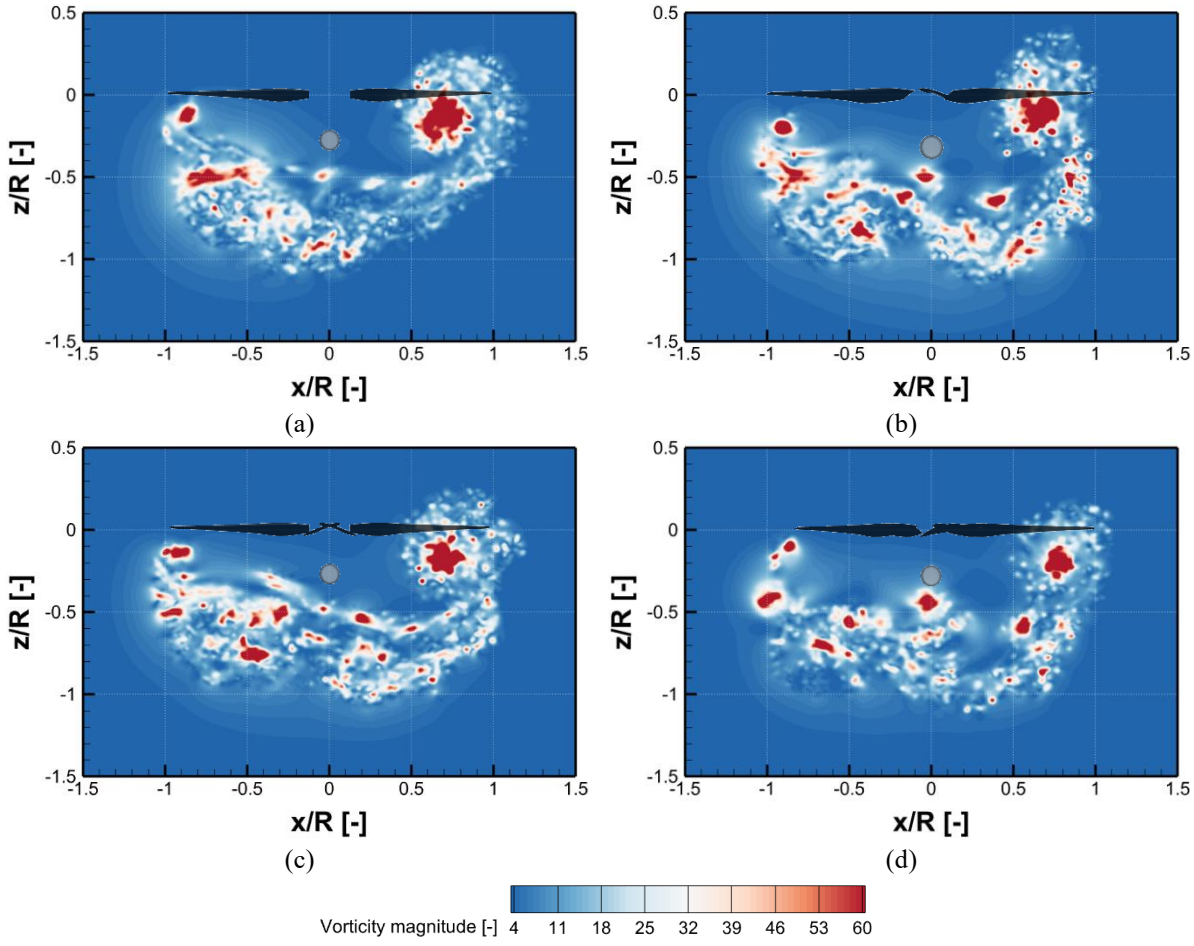

Fig. 11. Phase-averaged vorticity magnitude contours on the y–z plane at x/R = 3 under forward-flight conditions at ψ = 0°: (a) two-bladed, (b) three-bladed, (c) four-bladed, and (d) five-bladed configurations.

Fig. 11 presents the phase-averaged vorticity distributions on the x–z plane at $x/R = 3$ to further clarify the three-dimensional deformation of the wake. By removing cycle-to-cycle variability, the phase-averaged contours more clearly reveal the systematic differences in wake structure associated with blade number. The vorticity field was extracted at $x/R = 3$, where tip vortex roll-up and downstream wake deformation had developed sufficiently to enable a comparison of mature near-wake structures among blade-number configurations. Across all cases, the wake formed a rolled-up vortical distribution below the rotor disk as it convected downstream under forward-flight conditions. However, the distribution was asymmetric with respect to the rotor centerline. Specifically, the advancing side ($y/R > 0$) contained stronger concentrated vorticity than the retreating side ($y/R < 0$), reflecting the azimuthal loading asymmetry caused by the forward-flight inflow. This asymmetry was most evident in the two-bladed configuration, where higher blade loading produced stronger tip vortex structures on the advancing side and a clearer imbalance between the advancing- and retreating-side wake fields. As blade number increased, the high-vorticity regions associated with individual tip vortices weakened because per-blade loading decreased under the constant-thrust condition. Simultaneously, the reduced spiral-to-spiral distance promoted stronger interaction among adjacent vortices, making the individual tip vortex structures less distinct in the cross-plane. Consequently, the four- and five-bladed configurations exhibited a less coherent cross-plane wake organization than the two-bladed case, while the advancing–retreating-side asymmetry became less pronounced.

Fig. 12 presents the propeller thrust distributions on the rotor disk for different blade-number configurations under forward-flight conditions. Unlike under the hover condition, disk loading was characterized primarily by freestream-induced azimuthal inflow asymmetry. Consequently, all configurations exhibited a strongly nonuniform thrust distribution, with a high-loading region on the advancing side and a low-loading region on the retreating side. This loading asymmetry agrees with the y–z-plane wake structure in Fig. 11, where stronger vortical structures were observed on the advancing side because of the forward-flight inflow. The thrust distribution also reflected the blade-number effect. Under the constant-thrust condition, increasing blade number reduced per-blade loading; therefore, the peak thrust level decreased from the two- to five-bladed configurations. This reduction appeared as progressive weakening of the high-loading on the advancing side. Even in the higher blade-number configurations, however, disk loading remained asymmetric, indicating that forward-flight inflow asymmetry remained a dominant feature of propeller loading. A key difference from the hover condition was that the local loading enhancement associated with a blade passing directly over the airframe at $\psi = 0°$ was no longer the primary feature of disk loading. During hover, this loading increase was attributed to a local ground effect caused by blockage and upwash between the blade and the nearby cylindrical airframe. During forward-flight, by

contrast, the freestream convected the propeller wake downstream and spread the wake–airframe interaction over a broader streamwise region. Thus, propeller loading during forward-flight was determined mainly by the advancing–retreating-side imbalance and the inflow nonuniformity induced by the skewed wake rather than by a local propeller–airframe proximity effect.

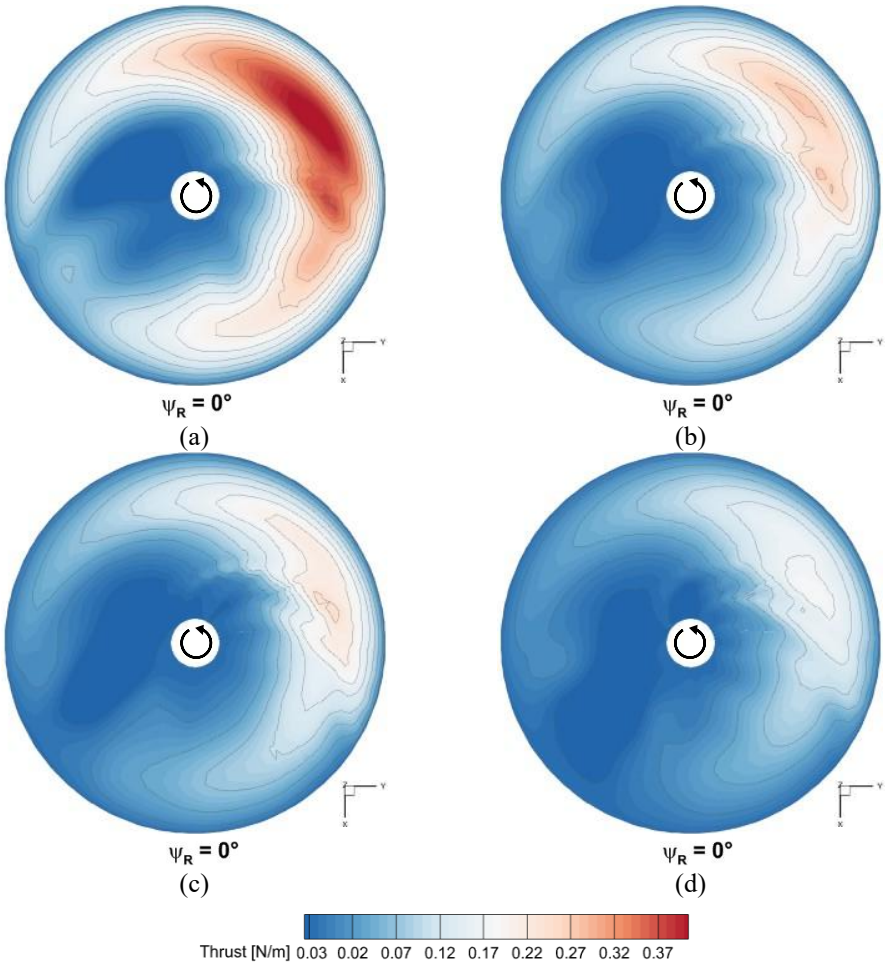

Fig. 12. Propeller thrust distributions over the rotor disk under forward-flight conditions for different blade-number configurations: (a) two-bladed, (b) three-bladed, (c) four-bladed, and (d) five-bladed configurations.

Fig. 13 presents the airframe surface pressure distributions and corresponding propeller wake structures represented by Lagrangian vortex particles for each blade-number configuration, providing insights into the streamwise development of the skewed wake over the cylindrical airframe. The depicted contour was obtained at ψ = 0°, when one blade passed over the airframe surface, and was viewed along the z-direction. In this wake visualization, the size of each vortex particle represents vortex strength; therefore, larger particles indicate stronger vortical structures. Consistent with the skewed wake evolution depicted in Figs. 10 and 11, the propeller wake was convected downstream and interacted with an extended streamwise portion of the airframe. For the two-

bladed configuration, large vortex particles appeared in the advancing-side wake, indicating strong vortical structures generated by higher per-blade loading. These coherent wake structures passed over and around the airframe, producing pronounced surface pressure variations along the cylinder. From the two- to four-bladed configurations, the surface pressure variation became less pronounced, indicating reduced wake-induced pressure loading on the cylindrical body. The five-bladed configuration, however, exhibited a different surface pressure response to the convected skewed wake. Although the vortex strength associated with each blade was reduced, the smaller spiral-to-spiral distance caused adjacent helical vortices to interact more strongly as they convected downstream. Consequently, the wake reaching the airframe became less organized and more spatially nonuniform, producing a surface pressure distribution that did not simply follow the attenuation observed from the two- to four-bladed configurations. This spatially irregular pressure response reflects the loss of coherent helical wake organization and the nonuniform impingement of the distorted wake on the airframe surface.

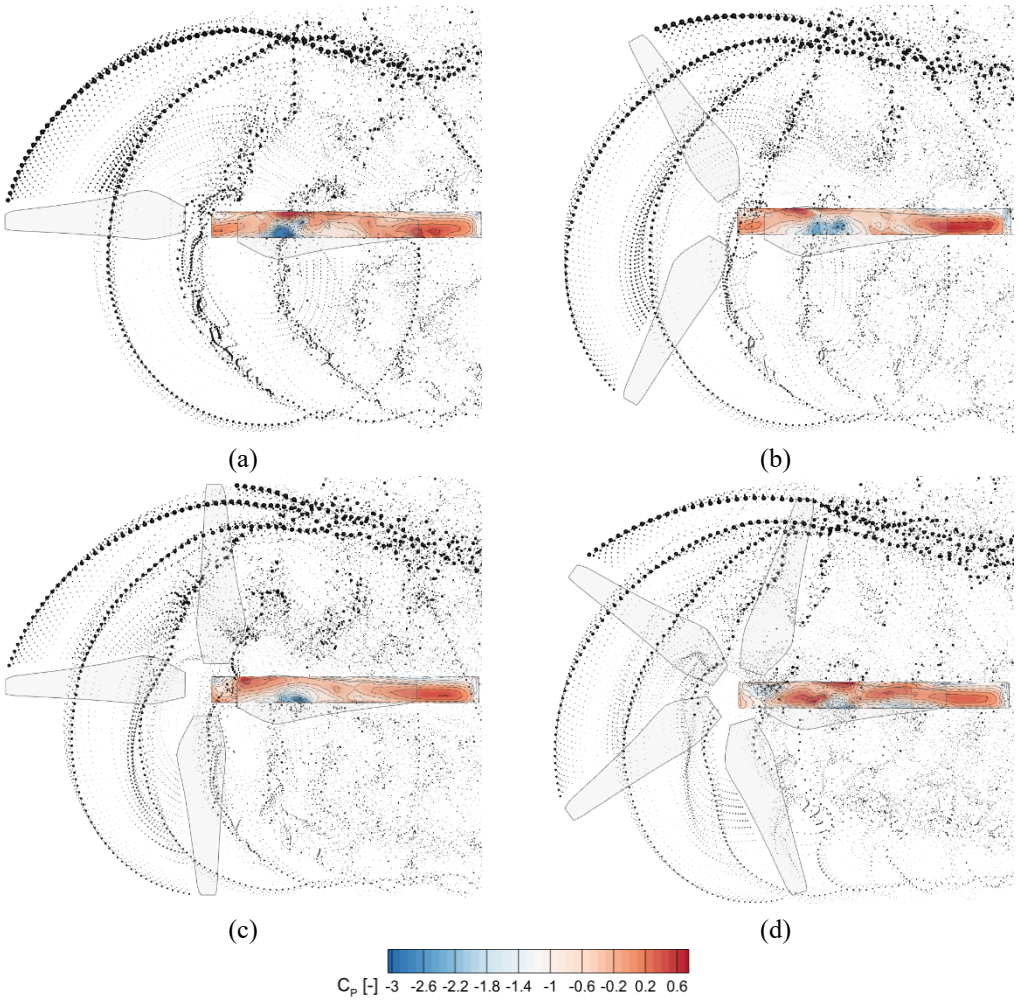

Fig. 13. Airframe surface pressure coefficient distributions and propeller wake structures represented by vortex particles under forward-flight conditions at $\psi = 0°$: (a) two-bladed, (b) three-bladed, (c) four-bladed, and (d) five-bladed configurations.

A comparison with the hover condition further clarified the change in the interaction mechanism. During hover, the airframe pressure variation was strongly associated with local blockage and upwash generated when a blade passed directly over the cylindrical body. Under forward-flight conditions, however, the skewed wake passed over and around the cylindrical airframe, and the surface pressure distribution in Fig. 13 primarily reflected the streamwise evolution of the wake and its local interaction with the airframe surface rather than the local blade–airframe proximity effect at $\psi = 0°$. This result indicates that, under forward-flight conditions, airframe loading arose primarily from the evolution of the skewed wake structure and the associated wake effects rather than from the instantaneous passage of a blade over the airframe.

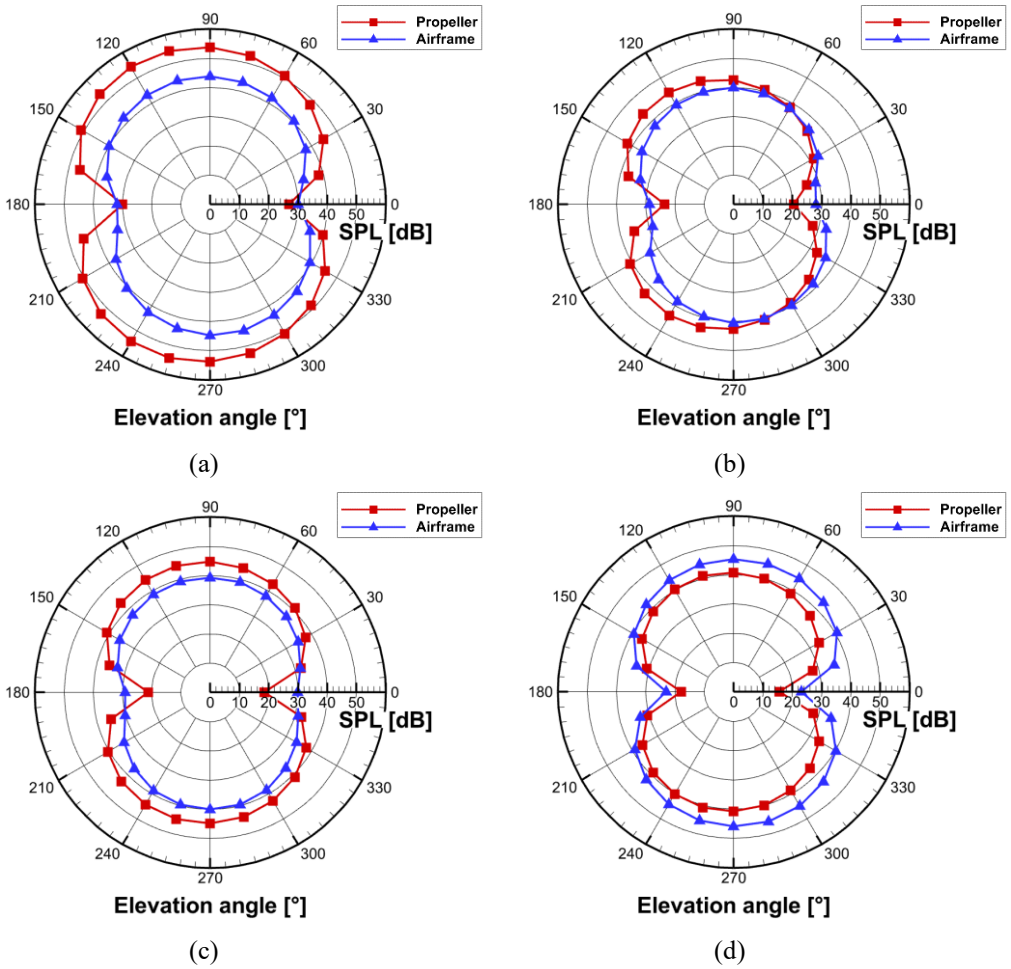

Fig. 14. Directivity of loading noise radiated from the propeller and cylindrical airframe under forward-flight conditions for different blade-number configurations: (a) two-bladed, (b) three-bladed, (c) four-bladed, and (d) five-bladed configurations.

Fig. 14 presents the predicted loading-noise directivity of the propeller and airframe under forward-flight conditions. A major difference from the hover condition was that the propeller contribution became more

prominent in forward-flight, particularly for the two-bladed configuration. As shown in Fig. 12, propeller disk loading was strongly asymmetric under forward-flight conditions, and this azimuthal loading imbalance became an important source of propeller loading noise. For the propeller contribution, the two-bladed configuration produced the highest loading-noise level over most elevation angles. As blade number increased, the reduced per-blade loading generally decreased the propeller loading-noise level similar to the hover condition, particularly in the three- and four-bladed configurations. In the five-bladed configuration, however, the decrease in per-blade loading did not induce a further reduction in propeller loading noise because the closely spaced wake structures in Figs. 10, 11, and 13 generated additional unsteady interaction. The airframe contribution also remained substantial under forward-flight conditions, although its generation mechanism differed from that in hover. Specifically, airframe loading noise arose from unsteady surface pressure loading produced by the downstream evolution of the skewed wake rather than from the local blade–airframe proximity effect observed in hover. Although the airframe contribution was generally lower than the propeller contribution in the two-bladed configuration, it became comparable to the propeller contribution at several elevation angles in the higher blade-number configurations.

Table VII compares the propeller and airframe OASPL contributions at $\theta = 270°$ under forward-flight conditions. For the two-, three-, and four-bladed configurations, the propeller contribution was larger than the airframe contribution, indicating that the forward-flight noise field was primarily influenced by the azimuthally asymmetric blade loading depicted in Fig. 12. As blade number increased, the total OASPL decreased from 52.68 dB in the two-bladed configuration to 46.53 dB and 43.44 dB in the three- and four-bladed configurations, respectively. Accordingly, the four-bladed configuration yielded the lowest total OASPL, corresponding to a 9.24 dB reduction relative to the two-bladed configuration. The five-bladed configuration, however, exhibited different acoustic behavior. Although this configuration had the lowest propeller OASPL, at 40.76 dB, the airframe OASPL increased to 45.87 dB and became the dominant contribution. Consequently, the total OASPL increased to 48.08 dB. This result indicates that the reduction in propeller loading noise was insufficient to reduce the total radiated noise when the airframe contribution increased. The increase in airframe noise aligns with the surface pressure fluctuations in Fig. 13. Therefore, the quantitative OASPL comparison indicates that the four-bladed configuration provided the most effective noise reduction under forward-flight conditions, whereas the five-bladed configuration introduced additional airframe noise induced by wake–airframe interaction despite the reduced propeller contribution.

Table VII. Comparison of predicted loading-noise levels under forward-flight conditions at $\theta = 270°$ for different blade-number configurations

	Two blades	Three blades	Four blades	Five blades
Propeller OASPL	53.76 dB	42.48 dB	44.69 dB	40.76 dB
Airframe OASPL	44.70 dB	40.48 dB	39.98 dB	45.87 dB
Total OASPL	52.68 dB	46.53 dB	43.44 dB	48.08 dB

Fig. 15 presents the far-field loading-noise spectra of the total, propeller, and airframe contributions at θ = 270° under forward flight conditions. Frequency is expressed in per-revolution order, and distinct components at the BPF and its harmonics are observed for all blade-number configurations. The relative propeller and airframe contributions, however, vary substantially with frequency. Although the aerodynamic loading required on each blade decreases as the blade number increases, the propeller spectrum does not decrease uniformly. In particular, the four-bladed configuration exhibits a higher SPL at the 4/rev BPF and at several higher-order components than the three-bladed configuration. This behavior indicates that the forward flight propeller noise is affected not only by the reduction in blade loading but also by the azimuthally nonuniform aerodynamic loading associated with the skewed wake and advancing–retreating side asymmetry. In the five-bladed configuration, the airframe contribution increases at several frequencies below the nominal 5/rev BPF, particularly over approximately 1–4/rev. These low-frequency components are consistent with the resolved wake motion and the resulting surface-pressure fluctuations on the airframe, which increase the airframe loading-noise contribution. A different spectral characteristic appears in the five-bladed configuration. The airframe contribution exceeds the propeller contribution at several frequencies below the nominal 5/rev BPF, particularly over approximately 1–4/rev. As discussed in the preceding wake and surface-pressure analyses, these low-frequency components are associated with the resolved low-frequency wake motion and the resulting variation in wake impingement on the airframe. The total spectra further show that the superposition of the propeller and airframe acoustic pressures varies with blade number. The total OASPLs of the two- and four-bladed configurations are 1.08 and 1.25 dB lower than their dominant propeller contributions, respectively, whereas those of the three- and five-bladed configurations exceed their dominant individual contributions by 4.05 and 2.21 dB. These results indicate net destructive superposition for the two- and four-bladed configurations and net constructive superposition for the three- and five-bladed configurations at the present observer location. These spectral and integrated acoustic results quantitatively support the phase-interference characteristics, as further examined in the acoustic pressure histories shown in Figs.

16 and 17. In summary, under forward flight conditions, the acoustic response reflects the combined effects of rotational-speed adjustment, azimuthally asymmetric loading blade loading, and skewed wake interaction. Although the lower rotational speed generally reduces propeller loading noise as the blade number increases, the enhanced BPF components in the four-bladed case and the increased sub-BPF airframe contribution in the five-bladed case demonstrate that the observed acoustic variations cannot be attributed to RPM scaling alone.

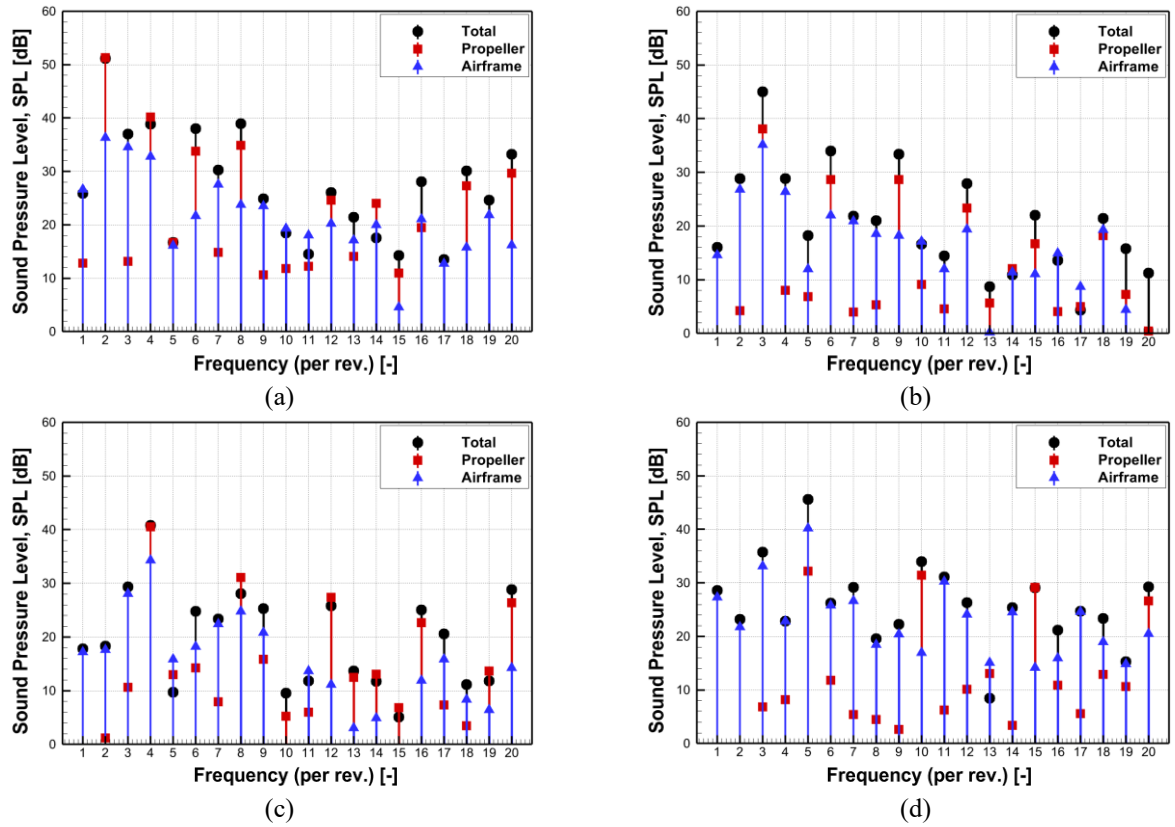

Fig. 15. Far-field loading-noise spectra of the total, propeller, and cylindrical airframe at $\theta = 270°$ under forward-flight conditions: (a) two-bladed, (b) three-bladed, (c) four-bladed, and (d) five-bladed configurations. Frequency is expressed in per-revolution order, where 1/rev represents one cycle per propeller revolution.

A distinct feature of the forward-flight results was that the total OASPL indicated a phase-dependent interaction between the propeller and airframe acoustic fields. In the two- and four-bladed configurations, the total OASPL values were 52.68 dB and 43.44 dB, respectively, which were lower than the corresponding propeller contributions of 53.76 dB and 44.69 dB. To clarify this phase-dependent acoustic interaction, the acoustic pressure histories at $\theta = 270°$ were analyzed together with the corresponding thrust-gradient distributions. The pressure signals were extracted over the final two propeller revolutions, during which the periodic loading-noise signature had fully developed. The propeller and airframe contributions were then examined separately to determine whether their acoustic pressure fluctuations were constructively or destructively superimposed at the observer

location. For the even-bladed configurations in Fig. 16, the propeller and airframe acoustic pressure signals exhibited a clear phase difference. In the two-bladed case, the propeller signal had a large-amplitude periodic fluctuation associated with the strong advancing–retreating-side loading imbalance, whereas the airframe signal was governed by unsteady pressure loading on the cylindrical surface induced by wake interaction. As depicted in Figs. 16(a) and (b), the acoustic pressure signals radiated from the propeller and airframe were approximately out of phase. Specifically, the positive pressure peaks of one component tended to coincide with the negative pressure peaks of the other, indicating partial destructive superposition of the two acoustic pressure fields. This phase opposition weakened the combined pressure signal and explains why the total OASPL was lower than the dominant individual contribution in the two- and four-bladed configurations.

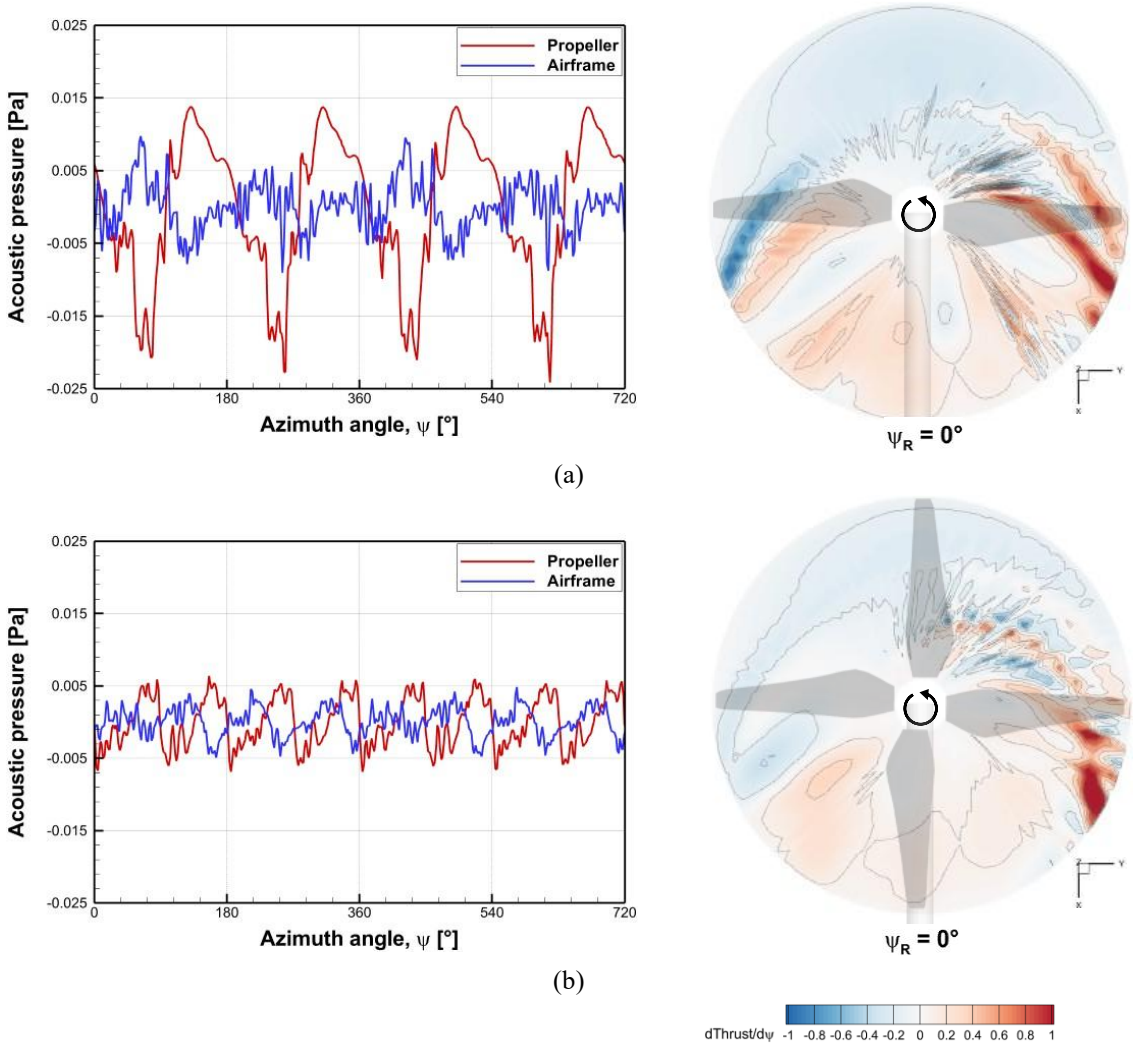

Fig. 16. Acoustic pressure histories and propeller thrust-gradient distributions for the even-bladed configurations under forward-flight conditions at $\theta = 270°$: (a) two-bladed and (b) four-bladed configurations.

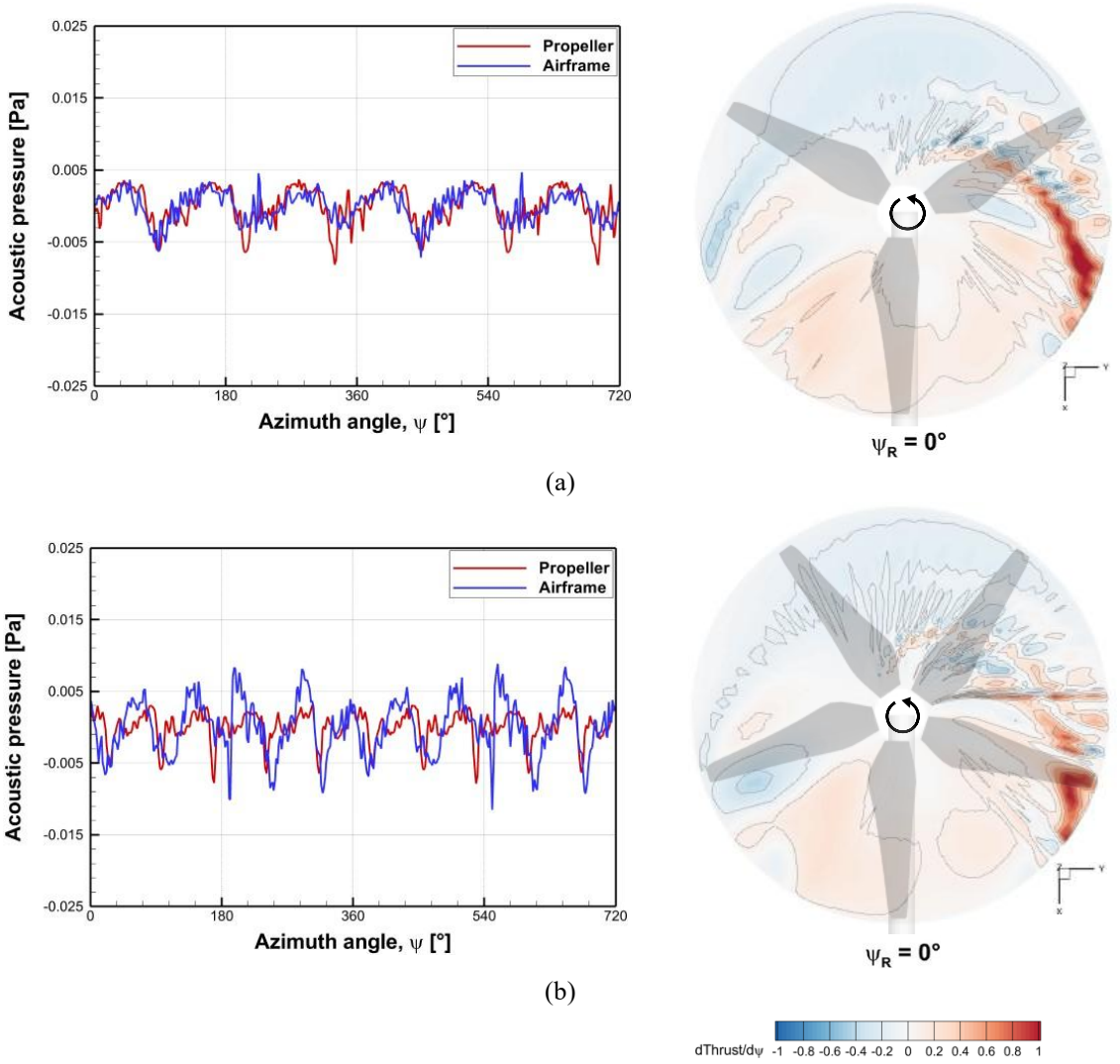

Fig. 17. Acoustic pressure histories and thrust-gradient distributions for the odd-bladed configurations under forward-flight conditions at $\theta = 270°$: (a) three-bladed and (b) five-bladed configurations.

As shown in Fig. 17, the acoustic pressure signals of the propeller and airframe had a different phase relation in the three- and five-bladed configurations. Specifically, in the three-bladed configuration, the pressure fluctuations from the two components were more closely phased over the two revolutions. Thus, the positive and negative phases of the acoustic pressure generated by propeller loading tended to align with the corresponding phases of the acoustic pressure radiated by unsteady loading on the airframe surface at $\theta = 270°$, resulting in constructive superposition at the observer location. The five-bladed configuration also exhibited overall tendency toward constructive superposition, although its pressure histories featured more irregular low- to mid-frequency fluctuations than those in the three-bladed case. This irregular fluctuation behavior is consistent with the spatially irregular wake–airframe interaction and severe surface pressure fluctuations shown in Fig. 13. Consequently, the total OASPL values of the three- and five-bladed configurations exceeded both component-wise contributions, as

shown in Table VII. These results indicate that the total loading noise under forward-flight conditions is determined not only by the individual acoustic levels of the propeller and airframe but also by the relative phase of their radiated pressure signals at the far-field observer [46].

The relative phase between the propeller- and airframe-generated acoustic pressures was further quantified from their complex Fourier coefficients at the first three BPF harmonics, as summarized in Table VIII. The phase difference is expressed between 0° and 180°; values approaching 0° indicate predominantly constructive superposition, whereas values approaching 180° indicate predominantly destructive superposition. The three-bladed configuration exhibits phase differences of 6.37°, 20.61°, and 2.56° at the first three BPF harmonics, indicating a predominantly in-phase relation. In contrast, the corresponding values for the four-bladed configuration are 139.92°, 154.56°, and 101.07°, showing a substantially more opposing phase relation. The two- and five-bladed configurations exhibit larger harmonic-to-harmonic variations, demonstrating that the acoustic interference is frequency dependent. The relative phase originates from the different temporal characteristics of the propeller and airframe aerodynamic loading. Under forward-flight conditions, the propeller contribution is primarily associated with the azimuthally nonuniform blade loading, whereas the airframe contribution arises from unsteady surface-pressure loading as the skewed wake passes over and around the cylindrical body. Changing the blade number modifies the azimuthal spacing between successive blades and the spacing between adjacent helical vortical structures. Consequently, the timing of the propeller loading fluctuations relative to the wake-induced airframe pressure fluctuations also changes within each revolution, producing different phase relations between the two acoustic contributions at the observer. The harmonic-to-harmonic variations in Table VIII therefore show that the even- and odd-blade behavior inferred from the integrated OASPL represents a net interference tendency for the present geometry, operating condition, and observer location, rather than a uniform phase relation at every harmonic.

Table VIII. Relative phase differences between propeller- and airframe-radiated acoustic pressures at θ=270° under forward-flight conditions.

	Two blades	Three blades	Four blades	Five blades
1st BPF	87.96°	6.37°	139.92°	9.42°
2nd BPF	162.86°	20.61°	154.56°	78.06°
3rd BPF	33.24°	2.56°	101.07°	114.10°

5. Conclusions

This study numerically examined wake evolution, aerodynamic interaction, and loading-noise generation in a propeller–airframe system with different blade numbers under hover and forward-flight conditions. Four fixed-pitch propeller configurations with two, three, four, and five blades were considered. A coupled vortex-based framework combining the source–doublet panel method with a time-accurate VPM was used to resolve the unsteady wake evolution and aerodynamic loading. The loading-noise component was predicted using the impermeable-surface formulation based on Formulation 1A of Farassat, with acoustic source surfaces defined on both the propeller blades and the cylindrical airframe.

Under hover conditions, increasing the blade number from two to four reduced the loading required on each blade, weakened the tip-vortex structures, and decreased the propeller and airframe loading fluctuations. The four-bladed configuration yielded the lowest total OASPL of 40.20 dB, corresponding to a 5.17 dB reduction relative to the two-bladed configuration. In the five-bladed case, the reduced spacing between adjacent helical vortices increased their mutual interaction and the associated low-frequency loading fluctuations, and the total OASPL increased to 45.84 dB. Under forward-flight conditions, the skewed wake and advancing–retreating side loading asymmetry altered the relative acoustic contributions of the propeller and airframe. The four-bladed configuration again produced the lowest total OASPL, 43.44 dB, representing a 9.24 dB reduction relative to the two-bladed case. For the five-bladed configuration, the propeller OASPL decreased from 44.69 to 40.76 dB relative to the four-bladed case, whereas the airframe OASPL increased from 39.98 to 45.87 dB. Consequently, the total OASPL increased to 48.08 dB, demonstrating that the increased airframe contribution can outweigh the reduction in propeller loading noise. Together, these findings offer physical insight into the unsteady aerodynamic interference, complex wake behavior, and noise characteristics of propeller–airframe configurations with different blade numbers. In particular, the present findings reveal that blade-number variation can trigger wake meandering, which drives pronounced low-frequency aerodynamic fluctuations. This complex wake dynamics fundamentally alter the acoustic contribution of the airframe, demonstrating that the airframe is not merely a passive body exposed to the wake, but an active source of unsteady loading and interactional noise.

However, the present study has several limitations. The aerodynamic framework is based on an inviscid, incompressible vortex formulation and therefore does not directly resolve viscous boundary layer development, flow separation, or turbulence generation near the propeller and airframe surfaces. The sensitivity of the predicted downstream wake evolution to vortex-particle regularization and numerical dissipation remains to be investigated.

Furthermore, the impermeable FW–H formulation predicts deterministic thickness and loading noise associated with resolved surface motion and unsteady aerodynamic loading, but it does not directly account for turbulence-related quadrupole noise, boundary layer noise, or separation-induced broadband noise. Nevertheless, the present results reveal that the blade-number effect in a propeller–airframe system is governed by a change in the dominant interaction mechanism rather than by a simple reduction in aerodynamic loading. In particular, reduced spacing between adjacent helical vortices strengthens wake–wake interaction and modifies wake impingement on the airframe, thereby reinforcing the role of the airframe contribution and phase-dependent acoustic superposition. Future extensions will integrate the current aerodynamic framework with CFD to employ a permeable-surface FW–H formulation, specifically aiming to account for flow-induced noise components arising from aerodynamic interactions.

Acknowledgments

This study was supported by the National Research Foundation of Korea (NRF) grant funded by the Ministry of Science and ICT (Project Number: RS-2025-25423496). This work was supported by the Glocal University 30 Project Fund of Gyeongsang National University in 2026.

Declaration of competing for interest

The authors declare that they have no known competing financial interests or personal relationships that could have appeared to influence the work reported in this paper.

References

[1] K.H. Goodrich, C.R. Theodore, Description of the NASA urban air mobility maturity level (UML) scale, in: AIAA Scitech 2021 Forum, 2021: p. 1627.

[2] N. EASA, Study on the societal acceptance of urban air mobility in Europe, European Union Aviation Safety Agency and McKinsey & Company (2021).

[3] M. Boucher, M. Rafaelof, D. Begault, A. Christian, S. Krishnamurthy, S. Rizzi, A psychoacoustic test for urban air mobility vehicle sound quality, in: INTER-NOISE and NOISE-CON Congress and Conference Proceedings, Institute of Noise Control Engineering, 2023: pp. 794–807.

[4] A.J. Torija, Z. Li, R.H. Self, Effects of a hovering unmanned aerial vehicle on urban soundscapes perception, Transp. Res. D Transp. Environ. 78 (2020) 102195.

[5] C. Kawai, J. Jäggi, F. Georgiou, J. Meister, R. Pieren, B. Schäffer, Short-term noise annoyance towards drones and other transportation noise sources: A laboratory study, J. Acoust. Soc. Am. 156 (2024) 2578–2595.

[6] C. Silva, W.R. Johnson, E. Solis, M.D. Patterson, K.R. Antcliff, VTOL urban air mobility concept vehicles for technology development, in: 2018 Aviation Technology, Integration, and Operations Conference, 2018: p. 3847.

[7] R. Piccinini, M. Tugnoli, A. Zanotti, Numerical Investigation of the Rotor-Rotor Aerodynamic Interaction for eVTOL Aircraft Configurations, Energies (Basel). 13 (2020).

[8] A. Zanotti, A. Savino, M. Palazzi, M. Tugnoli, V. Muscarello, Assessment of a Mid-Fidelity Numerical Approach for the Investigation of Tiltrotor Aerodynamics, Applied Sciences 11 (2021)

[9] D.S. Little, J. Majdalani, R.J. Hartfield, V. Ahuja, On the prediction of noise generated by urban air mobility (UAM) vehicles. I. Integration of fundamental acoustic metrics, Physics of Fluids 34 (2022).

[10] V. Ahuja, D.S. Little, J. Majdalani, R.J. Hartfield, On the prediction of noise generated by urban air mobility (UAM) vehicles. II. Implementation of the Farassat F1A formulation into a modern surface-vorticity panel solver, Physics of Fluids 34 (2022).

[11] M. Felli, R. Camussi, F. Di Felice, Mechanisms of evolution of the propeller wake in the transition and far fields, J. Fluid Mech. 682 (2011) 5–53.

[12] Y. Jo, T. Jardin, R. Gojon, M.C. Jacob, J.-M. Moschetta, Prediction of noise from low Reynolds number rotors with different number of blades using a non-linear vortex lattice method, in: 25th AIAA/CEAS Aeroacoustics Conference, 2019: p. 2615.

[13] D.C. Akiwate, P. Joseph, A. Parry, C. Paruchuri, On the balance between the tonal and broadband noise of isolated propellers, Int. J. Aeroacoust. 23 (2024) 122–153.

[14] P. Li, Y. Yang, Q. Li, E.J.G. Arcondoulis, B.R. Noack, Y. Liu, Effect of blade number on rotor efficiency and noise emission at hovering condition, Physics of Fluids 36 (2024).

[15] K. Baskaran, N.S. Jamaluddin, A. Celik, D. Rezgui, M. Azarpeyvand, Effects of number of blades on propeller noise, J. Sound Vib. 572 (2024) 118176.

[16] N.S. Zawodny, D.D. Boyd, Investigation of rotor–airframe interaction noise associated with small-scale rotary-wing unmanned aircraft systems, Journal of the American Helicopter Society 65 (2020) 1–17.

[17] J.M. Derlaga, C.W. Jackson, P.G. Buning, Recent progress in OVERFLOW convergence improvements, in: AIAA Scitech 2020 Forum, 2020: p. 1045.

[18] Y. Wu, M.J. Kingan, S.T. Go, Propeller–strut interaction tone noise, Physics of Fluids 34 (2022).

[19] J. Boyang, L. Weipeng, Experimental Study of the Rotor–Arm Interaction Noise in Single and Contra-Rotating Rotors of eVTOL Aircraft, J. Aerosp. Eng. 38 (2025) 4025023.

[20] L.R. Jiao, D. Peng, X. Wen, Y. Liu, J.W. Gregory, Experimental study of the interaction between rotor wake and a cylinder in Hover, in: 2018 Applied Aerodynamics Conference, 2018: p. 4214.

[21] S. Kim, Y.-H. Hwang, R.S. Myong, H. Lee, Interactional aerodynamics and acoustics of a rotor with an airframe in hover, Physics of Fluids 36 (2024).

[22] H. Lee, D.-J. Lee, Effects of platform motions on aerodynamic performance and unsteady wake evolution of a floating offshore wind turbine, Renew. Energy 143 (2019) 9–23.

[23] H. Lee, D.-J. Lee, Low Reynolds number effects on aerodynamic loads of a small scale wind turbine, Renew. Energy 154 (2020) 1283–1293.

[24] H. Lee, D.-J. Lee, Wake impact on aerodynamic characteristics of horizontal axis wind turbine under yawed flow conditions, Renew. Energy 136 (2019) 383–392.

[25] H. Lee, D.-J. Lee, Numerical investigation of the aerodynamics and wake structures of horizontal axis wind turbines by using nonlinear vortex lattice method, Renew. Energy 132 (2019) 1121–1133.

[26] H. Lee, B. Sengupta, M.S. Araghizadeh, R.S. Myong, Review of vortex methods for rotor aerodynamics and wake dynamics, Advances in Aerodynamics 4 (2022) 20.

[27] M. Park, H. Lee, Acoustic Analogy with High-Order Time Derivatives for Far-Field Acoustic Predictions, Acoust. Phys. 69 (2023) 844–852.

[28] S.M. Son, C.-H. Song, M.S. Araghizadeh, R.S. Myong, H. Lee, Investigation of aerodynamics, wake dynamics, and aeroacoustic characteristics of a full-configuration tiltrotor aircraft during transition flight, Physics of Fluids 37 (2025).

[29] H. Lee, D.-J. Lee, Rotor interactional effects on aerodynamic and noise characteristics of a small multirotor unmanned aerial vehicle, Physics of Fluids 32 (2020).

[30] M.S. Araghizadeh, B. Sengupta, H. Lee, R.S. Myong, Aeroacoustic investigation of side-by-side urban air mobility aircraft in full configuration with ground effect, Physics of Fluids 36 (2024).

[31] M.S. Araghizadeh, B. Sengupta, S.M. Son, H. Lee, R.S. Myong, Atmospheric turbulence inflow effect on the aerodynamics and aeroacoustics of side-by-side urban air mobility aircraft, Physics of Fluids 37 (2025).

[32] B. Sengupta, Y. Lee, M.S. Araghizadeh, R.S. Myong, H. Lee, Comparative Analysis of Direct Method and Fast Multipole Method for Multirotor Wake Dynamics, International Journal of Aeronautical and Space Sciences 25 (2024) 789–808.

[33] B. Sengupta, E. Esmaeilifar, M. Sadegh Araghizadeh, S. Kang, H. Lee, R.S. Myong, L. Prince Raj, Rotor-Fuselage-Intake Aerodynamics and Icing Using Vortex and Eulerian–Lagrangian Computational Fluid Dynamics Methods, AIAA Journal (2025) 1–22.

[34] G.S. Winckelmans, A. Leonard, Contributions to Vortex Particle Methods for the Computation of Three-Dimensional Incompressible Unsteady Flows, J. Comput. Phys. 109 (1993) 247–273.

[35] N.S. Zawodny, D.D. Boyd Jr, C.L. Burley, Acoustic characterization and prediction of representative, small-scale rotary-wing unmanned aircraft system components, in: American Helicopter Society (AHS) Annual Forum, 2016.

[36] P. Ventura Diaz, S. Yoon, High-fidelity computational aerodynamics of multi-rotor unmanned aerial vehicles, in: 2018 AIAA Aerospace Sciences Meeting, 2018: p. 1266.

[37] J. Malkki, Y. Yauwenas, C. Doolan, D. Moreau, Comparison of small rotor tonal and random noise decomposition methods, Acoust. Aust. 52 (2024) 323–337.

[38] G. Fasulo, G. Longobardo, F. De Gregorio, M. Barbarino, Experimental Acoustic Investigation of Rotor Noise Directivity and Decay in Multiple Configurations, Aerospace 12 (2025) 647.

[39] E. Moedersheim, M. Daghir, J.G. Leishman, Flow visualization of rotor wakes using shadowgraph and Schlieren techniques, NLR, 1994.

[40] J.G. Leishman, A. Bagai, Challenges in understanding the vortex dynamics of helicopter rotor wakes, AIAA Journal 36 (1998) 1130–1140.

[41] V.L. Okulov, I. V Naumov, R.F. Mikkelsen, I.K. Kabardin, J.N. Sørensen, A regular Strouhal number for large-scale instability in the far wake of a rotor, J. Fluid Mech. 747 (2014) 369–380.

[42] T. Leweke, H.U. Quaranta, H. Bolnot, F.J. Blanco-Rodríguez, S. Le Dizès, Long-and short-wave instabilities in helical vortices, in: J. Phys. Conf. Ser., 2014: p. 12154.

[43] F. Porté-Agel, M. Bastankhah, S. Shamsoddin, Wind-turbine and wind-farm flows: a review, Boundary. Layer. Meteorol. 174 (2020) 1–59.

[44] N. Belvasi, B. Conan, B. Schliffke, L. Perret, C. Desmond, J. Murphy, S. Aubrun, Far-wake meandering of a wind turbine model with imposed motions: an experimental S-PIV analysis, Energies (Basel). 15 (2022) 7757.

[45] D.H. Kim, C.H. Park, Y.J. Moon, Aerodynamic analyses on the steady and unsteady loading-noise sources of drone propellers, International Journal of Aeronautical and Space Sciences 20 (2019) 611–619.

[46] F. Sessini, D. Donnini, A. Chella, T. Schwarz, J. Yin, G. Bellani, E.L. De Angelis, Directional noise reduction via rotor phase–shifting for multirotor aircraft, Aerosp. Sci. Technol. (2026) 111699.